# How do variably striking faults reactivate during rifting? Insights from southern Malawi

Jack N. Williams[1*], Åke Fagereng[1]. Luke N. J. Wedmore[2], Juliet Biggs[2], Felix Mphepo[3], Zuze Dulanya[4], Hassan Mdala[3], Tom Blenkinsop[1]

[1]*School of Earth and Ocean Sciences, Cardiff University, Cardiff, UK*
[2]*School of Earth Sciences, University of Bristol, Bristol, UK*
[3]*Geological Survey Department, Mzuzu Regional Office, Mzuzu, Malawi*
[4]*Geography and Earth Sciences Department, University of Malawi, Zomba, Malawi*

*Corresponding author: Jack Williams (williamsj132@cardiff.ac.uk)

## Key points

- Stress states at the southern end of the Malawi Rift are tested by assessing fault reactivation potential.
- Variably oriented rift faults reactivate by all striking slightly obliquely to an E-W trending minimum principal compressive stress.
- Faults may locally accommodate pure normal dip-slip due to the presence of a deep seated crustal weakness.

## Abstract

Active normal faults at the southern end of the Malawi Rift follow an arcuate bend in the high grade metamorphic foliation, with strikes ranging from NW to NNE. However, previous estimates of the stress state that allows such a wide range of normal fault strikes to reactivate are enigmatic, as both a NW-SE and NE-SW trending minimum compressive stress ($\sigma_3$) have been proposed. Furthermore, we present field observations of a consistently N-S striking sub-vertical joint set in southern Malawi, which suggests an E-W trending $\sigma_3$. We address this problem by calculating the stress ratio ($\sigma_3/\sigma_1$, where $\sigma_1$ is the maximum compressive stress) and effective coefficient of friction ($\mu_s$') required to reactivate the rift's variably striking faults in stress states based on earthquake focal mechanisms (Stress State 1: $\sigma_3$=06/242) and joint sets (Stress State 2: $\sigma_3$=00/082). Given the consistency of joint orientations, we infer a uniform stress state and reject an alternative hypothesis that $\sigma_3$ rotates along the rift. In Stress State 1, NW-striking faults are well oriented. However, misoriented NNE-striking faults require $\mu_s$'<0.7 to reactivate, which is inconsistent with the lack of frictionally weak phyllosilicates detected in compositional analysis of these faults. In Stress State 2, all faults are well oriented and can reactivate at $\mu_s$'>0.6. This is also comparable to a previously reported geodetically-derived extension direction. Stress State 2 is therefore favoured, indicating that the southern Malawi Rift consists of a series of slightly-oblique basins, and not alternating orthogonal and highly-oblique sections as predicted by typical models of oblique rifting.



## Plain Language Summary

Stretching of the upper brittle part of the Earth's crust should be accommodated by cracks (faults) oriented at 90° to the stretching direction. However, this idealized scenario is rarely observed because the crust is often mechanically heterogenous, or because the stretching direction rotates over geological time. Thus, faults are often non-orthogonal (i.e. oblique) to the stretching direction. Here, we use a mechanical analysis to test the obliquity of faults in southern Malawi at the southern juvenile end of the East African Rift system where the crust is actively extending at ~2 mm/yr. This section is of interest as fault orientation varies along the rift, and a range of stretching directions have been proposed previously. Our mechanical analysis indicates that extension is most likely accommodated in southern Malawi by faults that are all slightly oblique to an E-W stretching direction. This is in contrast to previous models of oblique rifting, which suggest that stretching is accommodated by some faults at 90° to the stretching direction, whilst others are at a very low (<40°) angle to stretching.



## Key words

Continental rift, East African Rift, Fault reactivation, Tectonic stress, Normal faults, Stress inversions


## 1. Introduction

The axis of a continental rift is expected to be orthogonal to the minimum principal compressive stress ($\sigma_3$). This is, however, rarely the case [*Brune et al.*, 2018] due to factors such as temporal stress rotations since the inception of the rifting [*Bellahsen et al.*, 2006; *Henstra et al.*, 2015], or pre-existing crustal fabrics that present cohesionless [*Etheridge*, 1986; *Morley et al.*, 2004] or frictionally-weak planes [*Massironi et al.*, 2011]. These spatial

and temporal heterogeneities allow a much greater range of fault orientations, which strike oblique to $\sigma_3$ and do not contain the intermediate principal compressive stress ($\sigma_2$).

Often, obliquely oriented rifts will contain faults with a wide range of strikes, whereby some faults strike orthogonal to $\sigma_3$ and are linked oblique-slip or strike-slip transfer zones where faults striking highly obliquely to $\sigma_3$ [*Acocella et al.*, 1999; *Bellahsen & Daniel*, 2005; *McClay & White*, 1995; *Withjack & Jamison*, 1986], as has been proposed in the East African Rift [*Corti*, 2012; *Delvaux*, 2001], Rio Grande Rift [*Aldrich*, 1986], Rhine Graben [*Chorowicz & Deffontaines*, 1993; *Lopes Cardozo & Behrmann*, 2006], and the Gulf of Aden [*Bellahsen et al.*, 2006]. The stress directions in these rifts are typically inferred from measurements of incremental fault strain (i.e. fault slickensides, earthquake focal mechanisms). This is justified by the Wallace-Bott criterion, which predicts that fault slip is parallel to the direction of maximum resolved shear stress on a fault plane [*Bott*, 1959; *Wallace*, 1951]. However, this criterion can break down [*Pollard et al.*, 1993; *Twiss & Unruh*, 1998], including cases whereby rift faults that strike oblique to the regional $\sigma_3$ trend accommodate pure normal dip-slip [*Corti et al.*, 2013; *Morley*, 2010; *Petit et al.*, 1996; *Philippon et al.*, 2015]. Deriving stress states in rifts from fault-hosted slickensides is further complicated because dip-slip faults can host oblique-slip and even strike-slip components due to convergent patterns of co-seismic slip [*Hampel et al.*, 2013; *Philippon et al.*, 2015].

In this study, we address the problem of resolving stress states in rifts with variably striking faults by assuming *a priori* different stress states, and then interpreting their applicability in terms of fault reactivation potential. We use the southern end of the Malawi Rift (Figure 1) as a case example, as geological maps [*Bloomfield & Garson*, 1965; *Habgood et al.*, 1973; *Walshaw*, 1965], fault scarps [*Hodge et al.*, 2019; *Wedmore et al.*, in prep.], and earthquake focal mechanisms [*Delvaux & Barth*, 2010] demonstrate that active faults switch from dominantly NW-SE striking in the Makanjira Graben to NNE-SSW in the Zomba Graben and then back to NW-SE in the Lower Shire Graben as the rift follows an arcuate bend in the high grade metamorphic foliation (Figure 2). Furthermore, there is an inconsistency in the regional $\sigma_3$ trend when inferred from fault slickensides [*Chorowicz & Sorlien*, 1992], fault geometry [*Mortimer et al.*, 2007], earthquake focal mechanisms [*Delvaux & Barth*, 2010], and geodetic models [*Stamps et al.*, 2018]. Here, three possible stress states are considered:

- Stress State 1: A uniform stress state where $\sigma_3$ trends SW (06/242, Figure 2d), as proposed by an earthquake focal mechanism stress inversion for the Malawi Rift [*Delvaux & Barth*, 2010]. In this way, the angle ($\alpha$) between fault strike and $\sigma_3$ is ~90° for NW-striking faults, whilst for NNE-striking faults $\alpha$ is ~40°, and thus they would act as oblique transfer zones.
- Stress State 2: A uniform stress state with an ~E-W trending $\sigma_3$ (00/082, Figure 2e), which is consistent with the extension direction inferred from geodetic models [*Stamps et al.*, 2018] and regional joint orientations (Figure 2c). Thus, both faults sets form slightly oblique grabens $\sigma_3$ ($\alpha$>60°).
- Stress State 3: The stress state is heterogenous in southern Malawi, with Proterozoic fabrics actively rotating $\sigma_3$ along the rift so that $\alpha$ is consistently 90° (Figure 2f; *Morley*, [2010]).

We first compare these stress states to a new rift-wide stress inversion performed using an updated compilation of earthquake focal mechanisms and fault slickenside orientations. Then the reactivation potential of three differently oriented faults in these stress states is

determined in terms of their stress ratio, slip tendency, and effective coefficient of friction. By comparing these results to the frictional properties of the faults inferred from new field observations and compositional analysis, and deformation experiments performed by *Hellebrekers et al.*, [in review], we can determine which stress state is most applicable in southern Malawi. In doing so, new insights are gained into the applicability of using incremental fault strain measurements in stress inversions, and on the controls on fault geometry in an incipient rift.

## 2. Geological setting of the southern Malawi Rift

The Malawi Rift is a 900 km long amagmatic section of the East African Rift System's (EARS) Western Branch, and runs from the Rungwe Province in the north to the Urema Graben in the south (Figure 1; *Ebinger et al.,* [1987]). It is typically further divided along its axis into a series of 100-150 km long grabens and half grabens with alternating polarities [*Ebinger*, 1989; *Ebinger et al.*, 1987; *Flannery & Rosendahl*, 1990; *Laõ-Dávila et al.*, 2015]. The focus of this study are the three southernmost grabens: the Lower Shire, Zomba, and Makanjira Grabens (Figure 2a).

Basement rock within these grabens constitute part of the Southern Irumide Belt (Figure 1), a structurally complex Mesoproterozoic orogenic belt that underwent amphibolite-granulite facies metamorphism during the Pan African orogeny (c. 800-450 Ma.; *Kröner et al.,* [2001]; *Johnson et al.,* [2006]; *Fritz et al.,* [2013]). Whether this belt experienced earlier Irumide age deformation (c. 1020-950 Ma) is unclear [*Andreoli*, 1984; *Fritz et al.*, 2013; *Johnson et al.*, 2006; *Kröner et al.*, 2001] and the Lower Shire graben may strictly be part of the Neoproterozoic Zambesi Belt [*Chorowicz & Sorlien*, 1992; *Hargrove et al.*, 2003; *Laõ-Dávila et al.*, 2015]. The Lower Shire Graben also underwent NW-SE Karoo extension (Habgood, 1963; Castaing, 1991), whereas this extension was comparatively minor further north in the Zomba Graben [*Bloomfield*, 1965]. This was followed by a major period of Upper Jurassic-Lower Cretaceous magmatism throughout southern Malawi, which formed the Chilwa Alkaline Province [*Bloomfield*, 1965; *Castaing*, 1991; *Dulanya*, 2017; *Habgood*, 1963].

EARS extension initiated at the northern end of the Malawi Rift c. 8.6 Ma [*Ebinger et al.*, 1993], although a c. 25 Ma has also been proposed [*Mortimer et al.*, 2016; *Roberts et al.*, 2012]. Given the gradual southward propagation of the EARS [*Ebinger et al.*, 1987], the southern grabens analyzed here are likely younger (<5 Ma) than those further north; however, there is little chronostratigraphic control on their evolution [*Dulanya*, 2017; *Wedmore et al.*, in prep.]. As elsewhere in the EARS [*Versfelt & Rosendahl*, 1989], these grabens follow the trend of regional foliation (Figure 2a). Thus, a range of NW-NNE striking faults have formed in southern Malawi (Figure 2b). Topographic relationships demonstrate that both NW and NNE striking faults can dip in either direction orthogonal to strike (Figure 2a). Therefore, the range of fault orientations is polymodal [*Healy et al.*, 2015]; although given the lack of accurate measurements of fault dip, we cannot be sure if the range if strictly quadrimodal (four distinct clusters) or polymodal (continuous distribution of orientations).

## 3. Strain and stress indicators within the Malawi Rift

### *3.1 Previous estimates of strain and stress within the Malawi Rift*

At the scale of the EARS, kinematic models have been developed using a combination of earthquake slip vectors, and continuous and campaign GPS measurements [*Saria et al.*, 2014; *Stamps et al.*, 2008, 2018]. For southern Malawi, these models indicate an extension azimuth of 086°±5° relative to a fixed Nubia Plate [*Saria et al.*, 2014; *Stamps et al.*, 2018]. The current azimuth of the one continuous GPS station in southern Malawi (ZOMB) is 072° (Figure 2a; S*tamps et al.*, [2018]).

*Delvaux and Barth*, [2010] used an earthquake focal mechanisms stress inversion to derive a near Andersonian normal fault stress state for the Malawi Rift, with a sub-vertical maximum compressive principal stress ($\sigma_1$, 83/070) and sub-horizontal $\sigma_3$ (06/242). This $\sigma_3$ orientation implies NE-SW extension across the rift, in contrast to the E-W extension inferred from geodetic models [*Stamps et al.*, 2018]. Furthermore, this stress inversion predicts that NNE striking faults accommodate oblique extension (Figure 2d). However, slickensides on NNE striking faults indicate nearly pure dip-slip motion, and thus approximately NW-SE extension [*Bloomfield and Garson*, 1965; *Chorowicz and Sorlien*, 1992; *Wedmore et al.*, in prep.]. The geometry of faults from seismic reflection surveys within Lake Malawi have also been used to infer NW-SE rift extension [*Mortimer et al.*, 2007; *Scott et al.*, 1992].

### *3.2 An updated stress inversion for the Malawi Rift*

The discrepancy in rift extension direction when inferred from earthquake focal mechanisms, geodetic models, and fault slickensides may reflect the high azimuthal error and limited dataset (13 focal mechanism across the 900 km long rift) used in the *Delvaux and Barth*, [2010] stress inversion. We therefore update this stress field with an expanded dataset of 23 focal mechanisms (Table 1, Figure 1a), which incorporates: (1) subsequent seismicity such as the 2009 Karonga [*Biggs et al.*, 2010; *Hamiel et al.*, 2012] and 2018 Nsanje earthquake sequences [*U.S. Department of the Interior U.S. Geological Survey*, 2018], and (2) focal mechanisms from revised bodywave modelling [*Craig et al.*, 2011], which are considered more accurate than the Global Centroid Moment Tensor solutions used in the *Delvaux and Barth*, [*2010*] inversion (Table 1). As in *Delvaux and Barth*, [2010], we use Win-Tensor (version 5.8.8, *Delvaux and Sperner*, [2003]) to perform the inversion. Here, the data are first processed using the "Right Dihedron Method" to determine the possible range of $\sigma_1$ and $\sigma_3$ orientations [*Angelier & Mechler*, 1977]. This range is then refined by using "Rotational Optimisation" [*Delvaux & Sperner*, 2003], which seeks to reduce the misfit angle ($\omega$) between the earthquake slip vectors and the azimuth of maximum shear stress within the inversion. This inversion is first run for both nodal planes and then subsequently with just the plane that has the smallest misfit. Focal mechanisms were progressively filtered during the Right Dihedron Method analysis using the Counting Deviation method *(Delvaux and Sperner*, [2003], see supplementary information S1), and then by removing cases where $\omega$>45° for both nodal planes during Rotational Optimisation.

The revised stress field shows a slight clockwise rotation of $\sigma_3$ to 12/070 relative to the *Delvaux and Barth*, [2010] inversion (Figure 3). This $\sigma_3$ azimuth thus lies approximately halfway between those derived in Stress States 1 and 2 and is still inconsistent with NW trending slickensides. Notably, however, the azimuthal accuracy has been improved (from $\omega$=±22° to ±12°). This may reflect that *Delvaux and Barth*, [2010] included all focal mechanisms in their inversion regardless of whether they were compatible with each other,

whilst our expanded dataset allowed a more selective approach. Stress inversions combining fault slickensides [*Chorowicz and Sorlien*, 1992; *Wedmore et al.*, in prep.] and earthquake focal mechanisms were also attempted. However, these could not produce a reliable reduced stress tensor as either the data filtering was too severe, or the resulting stress shape ratio ($\Phi=\sigma_2-\sigma_3/\sigma_1-\sigma_3$) indicates an unrealistic prolate stress ellipsoid ($\Phi=0.04$, *Lisle et al.*, [2006]; see Supplementary Information S1). In summary, the updated stress inversions for the Malawi Rift cannot distinguish between the three stress states for southern Malawi postulated in the introduction. Hence, there is a need to consider other indicators of stress and strain within the rift, and to assess fault reactivation potential in different stress states.

### *3.3 Joint orientations*

Figures 2 and 4 show the orientations of two steeply-dipping joint sets in southern Malawi, which strike N-S and E-W. N-S striking joints have bare surfaces and are mutually cross cutting with the E-W striking set, though tend to cut across them more commonly than vice-versa. The majority of measurements were taken within the Zomba Graben; however, the N-S and E-W sets are also observed at two locations within the Makanjira Graben (Figure 2). Joint orientations were all measured >50 m from faults and are inferred to be outside their respective damage zones.

By inferring that these joints are opening parallel to the trend of $\sigma_3$, it is possible to derive another estimate for its orientation within southern Malawi. To do this, we quantitatively analyse joint orientations using Kamb Contours (Figure 4a), where contours represent standard deviations away from the expected density of a random sample [*Kamb*, 1959]. This analysis finds that the trend of the highest concentration of poles to the N-S striking joint set trends 082°±7°, which is taken here as the joint-derived $\sigma_3$ trend. This trend indicates an extension direction that is within error of the geodetically-derived extension direction for the Malawi Rift [*Saria et al.*, 2014; *Stamps et al.*, 2018]. The E-W striking joints are interpreted to reflect either: (1) an orthogonal joint set to the N-S set, and/or (2) the emplacement of E-W striking Chilwa Akaline Province dykes [*Bloomfield*, 1965]. Many of the N-S striking joints are foliation-parallel and thus may not necessarily reflect tectonic stresses [e.g. *Price*, 1959; *Engelder*, 1985; *Williams et al.*, 2018]. However, the N-S striking joint set is also observed within isotropic rocks, and so the $\sigma_3$ trend is not significantly changed when foliation-parallel joints are removed from the analysis (079°±8°, Figure S4).

## 4. Fault strength in southern Malawi

To calculate fault reactivation potential at the southern end of the Malawi Rift, it is necessary to the consider the frictional properties of its faults. We therefore selected three faults (Thyolo, Chingale Step, and Bilila-Mtakataka, Figure 2a), which: (1) encompass the range of fault orientations observed in southern Malawi, (2) have late-Quaternary fault scarps, and are therefore considered active (*Jackson and Blenkinsop*, 1997; *Hodge et al.*, 2018, 2019; *Wedmore et al.*, in prep.], and (3) are well-exposed, so it is possible to sample them for compositional analysis. The footwalls of the Chingale Step and Thyolo faults consist of intensely fractured basement, which is in contact with the hanging wall post-Miocene sediments (Figure 5; *Dulanya*, [2017]). The contact itself consists of a <1 m thick fault gouge (Figure 5). Along most of its length, the Bilila-Mtakataka fault consists of a soil-mantled scarp [*Hodge et al.*, 2018; *Jackson & Blenkinsop*, 1997]. However, at Kasinje (Figure 2a), the fault consists of a 3 m thick unit of intensely fractured gneiss that separates footwall and hanging wall hornblende gneisses [*Hodge et al.*, 2018].

To assess the composition of the fault zones, X-ray diffraction (XRD) analyses were conducted on two samples from each of the faults: (1) a 'country rock' sample from the intact protolith closest to the fault, and (2) a 'fault rock' sample from the faulted contact itself, i.e. the fault gouge for the Thyolo and Chingale Step faults (Figure 5), and intensely fractured gneiss for the Bilila-Mtakataka fault. XRD patterns were collected on powdered samples with a Philips PW1710 Automated Powder Diffractometer using Cu-Kα radiation at 35kV and 40mA, between 2 and 70° 2θ, at a scan speed of 0.04 °2θ/s. From the scans, phases were identified using Philips PC Identify software. Using the peak areas, semi-quantitative analysis was then performed to estimate the weight percentage of each identified phase (Table 2, Figure S5).

For each fault, we find that the phyllosilicate content is <15% (Table 2). This is significant as faults that are frictionally weak (fault static coefficient of friction ($\mu_s$)<0.4) typically contain interconnected phyllosilicates phases that constitute >30-40% of the fault rock [*Massironi et al.*, 2011; *Moore & Lockner*, 2004]. Thus, we infer that these faults exhibit 'Byerlee' frictional strengths ($\mu_s$~0.6-0.8; *Byerlee*, [1978]), which is also consistent with the results of deformation experiments on a suite of basement lithologies from the Malawi Rift ($\mu_s$=0.55-0.80; *Hellebrekers et al.*, [in review]). There are non-systematic differences in composition between some footwall country rock and fault rock samples (Table 2). For example, the Chingale Step fault gouge is near pure calcite, yet this phase is not detected in its country rock sample. These samples alone, however, are insufficient to determine if these differences reflect local protolith variations, near-surface weathering [*Isaacs et al.*, 2007], or fault zone alteration [*sensu Sutherland et al.*, 2012].

## 5. Fault reactivation potential analysis in southern Malawi

Fault reactivation potential considers how susceptible a fault, of a given orientation and stress state, is to slip under the Mohr-Coulomb failure criterion. This criterion describes the shear stress ($\tau$) required for a fault to exceed its frictional resistance:

$$\tau = c + \mu_s(\sigma_n - P_f) \quad (1)$$

where $\sigma_n$ is the normal stress, $c$ is the cohesive strength, and $P_f$ is pore fluid pressure. We consider fault reactivation in potential in southern Malawi in terms of Stress Ratio, Slip Tendency, and effective coefficient of friction (Figure 6).

### *5.1. Stress ratio*

The stress ratio is the ratio between $\sigma_3$ and $\sigma_1$ required for fault slip ($Q$=$\sigma_3/\sigma_1$, Figure 6; *Sibson*, [1985]). For the faults considered here, which strike obliquely to $\sigma_3$ and do not contain $\sigma_2$, we use the 3D solution outlined by *Leclère and Fabbri*, [2013], where:

$$Q = \frac{-(2AD\mu_s + 2C) \pm \sqrt{\Delta}}{A^2{\mu_s}^2 - C} \quad (2)$$

Here, *A, B, C, D* and $\Delta$ are functions defined by the stress shape ratio ($\Phi$), $c$, $\mu_s$, magnitude of $\sigma_1$, and the direction cosines between the normal to the fault plane and the three principal stress axes (see supplementary information S2). $Q$ and $\mu_s$ must be real numbers with $Q \leq 1$ and $\mu_s \geq 0$ [*Leclère & Fabbri*, 2013].

We calculate *Q* for the three faults described in section 4, given Stress States 1 and 2. For Stress State 1 ($\alpha$ is ~90° for NW-striking faults and ~40° for NNE-striking faults) we use the principal stress orientations derived in the *Delvaux and Barth,* [2010] stress inversion ($\sigma_1$=83/070, $\sigma_2$=02/333, $\sigma_3$=06/242), whilst for Stress State 2 ($\alpha$ is ~60° for all faults) the principal stress orientations are based on joint orientations ($\sigma_1$=90/000, $\sigma_2$=00/172, $\sigma_3$=00/082). No reactivation analysis is conducted for the stress rotation hypothesis (Stress State 3), as it intrinsically assumes that all faults are optimally oriented for failure [*Morley*, 2010].

The strike of the Chingale Step and Thyolo faults is well constrained from their prominent scarps that are visible in a 12 m resolution TanDEM-X digital elevation model [*Hodge et al.,* 2019; *Wedmore et al.,* in prep.] . For the Chingale Step fault, the strike is the orientation of the line that connects the two ends of its scarp, whilst for the segmented Thyolo fault, strike is the orientation of its longer north-western section (Figure 2a). The Bilila-Mtakataka fault is best described by two sub-parallel segments, the longest of which is oriented 156/46 NE [*Hodge et al.*, 2018]. Dips of 57° and 60° for the Chingale and Thyolo faults were derived from field measurements (Figure 5). Although there is an uncertainty in how representative these surface measurements of fault dip are, these measurements are similar to those inferred at depth from geophysical surveys elsewhere in the Malawi Rift (45-65°; *Wheeler and Rosendahl,* [1994]; *Mortimer et al.,* [2007]; *Kolawole et al.,* [2018]).

As justified in section 4, we infer that these faults exhibit Byerlee frictional strengths, and so a value of $\mu_s$=0.7 is used. A foliation-parallel pre-existing fault would generally be considered cohesionless [*Morley et al.*, 2004; *Sibson*, 1985]. However, the high-grade metamorphic fabrics within the Malawi Rift are qualitatively observed to be cohesive (Figure 4b). Furthermore, the low rift strain rates (~2 mm/yr; *Saria et al.,* [2014]) imply that there are long recurrence intervals between earthquakes, so it is possible that interseismic healing has led to a recovery of some fault cohesion [*Tenthorey & Cox*, 2006]. To account for this ambiguity, we calculate *Q* for end-member cases where $c$=0 and $c$=40 MPa, the latter of which is derived from crystalline rocks typically exhibiting tensile strengths ($T_0$) of 20 MPa, and that $c \approx 2T_0$ [*Lockner*, 1995; *Sibson*, 1985, 1998].

No knowledge of stress magnitudes is required for calculating *Q* for a cohesionless fault [*Leclère & Fabbri*, 2013]. However, the magnitude of $\sigma_1$ is needed to determine *Q* for a cohesive fault, which is calculated by assuming an Andersonian normal fault stress state where:

$$\sigma_1 = \sigma_v = \bar{\rho}(z) g z \quad (3)$$

where $\sigma_v$ is the vertical stress, $g$ is gravity (9.8 $ms^{-2}$), $z$ is depth, and $\bar{\rho}(z)$ is the average density of the overlying crust for a given depth, which is a function of a Malawi Rift three-layer crustal model (Table S2; *Nyblade and Langston,* [1995]; *Fagereng,* [2013]). As *Q* will vary with depth for a cohesive fault, it is calculated here between 6-35 km, which encompasses the depth range for instrumentally-recorded earthquake nucleation in the Malawi Rift [*Biggs et al.*, 2010; *Craig et al.*, 2011; *Nyblade & Langston*, 1995].

We assume the pore fluid pressure, $P_f$ =0; however, the influence of fluids on fault reactivation is assessed in section 5.3. The stress shape ratio ($\Phi$) is 0.33, as derived from the

updated stress inversion (Figure 3). For comparison, the orientation of the faults is shown in a stereoplot that is contoured by *Q* values for a given set of Φ, $\mu_s$, principal stress orientations, and (for cohesive faults) depth. To allow for the uncertainty in Φ and $\mu_s$, *Q*-contour plots are also constructed in Φ-$\mu_s$ space for a fixed set of fault and principal stress orientations [*Boulton et al.*, 2018].

### *5.2 Slip tendency*

Slip tendency ($T_s$) is a measure of the ratio of τ to $\sigma_n$ acting on the fault surface [*Lisle & Srivastava,* 2004; *Morris et al.*, 1996]:

$$T_s = \frac{\tau}{\sigma_n} \tag{4}$$

For a given stress state, there is a maximum value of $T_s$, which is that acting on a cohesionless optimally-oriented fault (Figure 6; *Lisle and Srivastava,* [2004]). This leads to the definition of a normalized index of slip tendency ($T'_s$) that ranges between 0-1:

$$T'_s = \frac{T_s}{\max(T_s)} = \frac{\tau}{\sigma_n tan\phi} \tag{5}$$

(corrected from eq. 3 in *Lisle and Srivastava,* [2004]; pers. comm. R. Lisle) where ϕ is the angle of internal fault friction (tanϕ=$\mu_s$). A fault with low $T'_s$ thus also reactivates at low *Q* (Figure 6). To calculate $T_s$ and $T'_s$ for the Chingale Step, Thyolo and Bilila-Mtakataka faults without knowledge of the magnitudes of τ and $\sigma_n$, we use the solutions outlined by *Lisle and Srivastava,* [2004] (see supplementary information S3). This analysis is performed for Stress States 1 and 2, assuming $\mu_s$=0.7, $P_f$=0, and Φ = 0.33.

### *5.3 Fault effective coefficient of friction*

The concept of $T_s$ can be extended to calculate the effective coefficient of friction ($\mu_s$'), which describes the maximum value of $\mu_s$ or lowest value of $P_f$ that allows faults to reactivate for a given stress state, without also inducing failure along optimally oriented planes in intact rock (Figure 6; *Sibson,* [1985]; *Muluneh et al.*, [2018]). Like $T_s$, $\mu_s$' is a measure of the ratio of τ to $\sigma_n$ acting on a fault, however, it is derived using inferred principal stress magnitudes, and fault cohesion can be incorporated. This is advantageous as $\mu_s$' can then be compared to values of $\mu_s$ inferred from experimental and compositional analysis of faults to determine if they will reactivate in a given stress state, or if elevated fluid pressures are required for reactivation.

Principal stress magnitudes can be derived as $\mu_s$' is being equated to the stresses acting on an optimally oriented fault (Figure 6). In this case, the relative principal stress magnitudes can be calculated using Mohr-Coulomb theory [*Jaeger et al.*, 2007]:

$$\sigma_1 = 2c\sqrt{\frac{1+\sin\phi_{intact}}{1-\sin\phi_{intact}}} + \sigma_3\left(\frac{1+\sin\phi_{intact}}{1-\sin\phi_{intact}}\right) \tag{6}$$

where $\phi_{intact}$=$\tan^{-1}\mu_{s\text{-}intact}$, and $\mu_{s\text{-}intact}$ is the frictional strength of intact rock. Given the results of *Hellebrekers et al.,* [in review], we take $\mu_{s\text{-}intact}$ to equal 0.7, thus $\phi_{intact}$=35° and is the same

as the fault frictional strength ($\mu_s$). Since $\sigma_1$ can be derived from eq. 3, it is thus also possible to calculate $\sigma_3$ and $\sigma_2$ by rearranging eq. 6 and the equation for $\Phi$ (eq. S1) respectively. The principal stress magnitudes can then be used to calculate $\tau$ and $\sigma_n$ as a function of depth [*Jaeger et al.*, 2007], and $\mu_s$' can be derived by rearranging the Mohr Coulomb criterion (eq. 1). Thus, for the parameters assumed here:

$$\mu_s'(z) = \frac{\sqrt{C\left(\frac{2.7z\bar{\rho}(z)-42}{9.8z\bar{\rho}(z)}\right)^2 - 2C\left(\frac{2.7z\bar{\rho}(z)-42}{9.8z\bar{\rho}(z)}\right) + C} - \frac{c}{\sigma_1}}{A\left(\frac{2.7z\rho(z)-42}{9.8z\bar{\rho}(z)}\right) + B} \quad (7)$$

where the functions *A*, *B*, and *C* are defined by equations S2-S4 (see supplementary information S4). As previously, we calculate $\mu_s$' for the Thyolo, Chingale Step, and Bilila-Mtakataka faults being reactivated in Stress States 1 and 2 over a depth range of 6-35 km and consider both cohesionless and cohesive faults. If $\mu_s$' and $\mu_{s\text{-intact}}$ are set to be the same, then the minimum pore fluid pressure ($P_f$') required to reactivate a fault (Figure 6) can be calculated from $\mu_s$' as a function of depth:

$$P_f(z) = \sigma_n(z) - \left(\frac{\sigma_n(z)\mu_s'(z)}{\mu_s}\right) \quad (8)$$

(see supplementary information S4). This is calculated with $\mu_s$=0.7 and is plotted in terms of the effective pore-fluid factor ($\lambda_v$'=$P_f$'/$\sigma_v$). In addition, we show the results of this analysis at a depth of 20 km in 3D Mohr Space using MohrPlotter v. 2.8.3 [*Allmendinger et al.*, 2013].

## 6. Fault reactivation potential results

The Thyolo and Bilila-Mtakataka faults have a high reactivation potential under Stress State 1, as their *Q* value is 'favourable' ($Q$>0.5$Q_{Optimal}$, Figures 6b and 7; *Sibson*,[1985]; *Leclère and Fabbri*, [2013]), and $T'_s$~1 (Table 3, Figure S6). Thus, they will reactivate under Stress State 1 at relatively high $\mu_s$' (>0.55), regardless of whether they are cohesive or not (Table 3, Figures 8 and 9a). Conversely, the Chingale Step fault is 'unfavourably' (0.5$Q_{Optimal}$>$Q$>0; Figures 6c and 7a) to 'severely misoriented' ($Q$<0 Figures 6d and 7c) in this stress state, depending on depth and whether it is cohesive or not. $T'_s$ =0.67 (Table 3), and at depths >10 km, will not reactivate in Stress State 1 unless $\mu_s$'<0.7 or $\lambda_v$'>0.1 (Table 3, Figures 8b, 9, and S7b).

In Stress State 2, all faults are favourably oriented (Figure 6b) and exhibit $T'_s$>0.8, although the reactivation potentials of the Thyolo and Bilila-Mtakataka faults are slightly less than under Stress State 1 (Table 3). In Stress State 2, all faults will reactivate at $\mu_s$>0.5 at depths >10 km (Table 3, Figures 8 and 9b). All results for *Q* are broadly independent of the values of $\Phi$ and $\mu_s$ used in this analysis (Figures 10 and S8).

## 7. How do faults in southern Malawi reactivate?

Although the Thyolo and Bilila-Mtakataka faults are well oriented in Stress State 1, the Chingale fault in the Zomba Graben is unfavourably to severely misoriented (Table 3). Late Quaternary activity on this fault has been demonstrated by *Wedmore et al.*, [in prep.], and so

its orientation is representative of a structure currently accommodating extension in this region. To reactivate as a cohesionless fault under Stress State 1 at 10-35 km depth -the depth range at which the majority of earthquakes nucleate in the Malawi Rift (Table 1)- $\mu_s$' ranges between 0.5-0.7 (Figure 8b). This is at the lower end of frictional strengths inferred from its composition (Table 2) and deformation experiments on basement rocks in Malawi [*Hellebrekers et al.,* in review]. In the cohesive fault case, $\mu_s$'<0.45 (Figure 8b), and so below its likely frictional strength.

Alternatively, the Chingale fault may reactivate under Stress State 1 at $\mu_s$=0.7 through an increase in fluid pressure ($\lambda_v$'<0.2, Figure S8). These fluid pressures are sustainable in a normal fault stress state [*Sibson & Rowland*, 2003]. However, the crust in the Malawi Rift has been dehydrated during one or more episodes of high grade metamorphism, and is therefore likely to be comparatively dry [*Fagereng,* 2013]. Furthermore, where faults do host high fluid pressures, they often contain extensive vein networks [e.g. *Bruhn et al.,* 1994; *Caine et al.,* 2010; *Sutherland et al.,* 2012], which are not observed in the fault zones we considered (Figures 4b and 5).

We emphasise that this reactivation analysis cannot definitively discount any of the possible stress states assessed here. Ideally, stress orientations would be measured using a range of techniques (e.g. borehole breakouts). Nevertheless, if we assume frictionally strong faults and cohesive high grade metamorphic fabrics, then it is difficult to account for why a structure with the NNE-SSW strike of the Chingale Step fault (or indeed other similarly-oriented faults in the Zomba Graben, Figure 2a) would have activated and continue reactivating in Stress State 1, instead of a more optimally oriented fault forming. Conversely, all faults are favourably oriented in Stress State 2, and so can reactivate at $\mu_s$ or $P_f$ that require neither frictionally weak minerals nor elevated fluid pressure (Figure 8). Furthermore, this stress state is consistent with joint orientations and the geodetically-derived extension direction [*Stamps et al.*, 2018].

Under the Wallace-Bott criterion, southern Malawi accommodates NE-SW extension in Stress State 1 (Figure 2d) or E-W extension in Stress State 2. It is thus difficult to reconcile these stress states to the range of NW-SE to NE-SW extension directions have been proposed (see Section 3.1). Notably, however, fault slickensides and earthquake focal mechanisms in the Zomba Graben (Table 1, Figure 5; *Chorowicz and Sorlien,* [1992]; *Wedmore et al.,* in [prep.]) indicate NW-SE extension, in contrast to the highly oblique ($\alpha$<40°) NE-SW extension predicted by applying the Wallace-Bott criterion to Stress State 1.

A range of extension directions can be accounted for by the model proposed in *Morley,* [2010] where pre-existing Southern Irumide metamorphic fabrics rotate $\sigma_3$ along the southern Malawi rift, so that all faults are pure dip-slip (i.e. Stress State 3, Figure 2f). In this way, all faults will be optimally oriented for reactivation. Furthermore, although some oblique-slip focal mechanisms (Table 1) and fault slickensides (Figure S2) are recorded in southern Malawi, in the former case, these tend to be historical focal mechanisms that were not instrumentally well-recorded, whilst with regards to the latter, this may relate to slickensides that record the inherent oblique slip component of normal faulting earthquakes as the fault tip is approached [*Hampel et al.*, 2013; *Philippon et al.*, 2015]. There is, however, a discrepancy between this hypothesis and the homogenous orientation of joint sets in southern Malawi Rift, which suggest a uniform stress state (Figure 2 and 4). The Bilila Mtakataka and Chingale Step faults also locally cross-cut the foliation in a non-systematic manner at the

surface (Figure 2a; *Bloomfield,* [1965]; *Jackson and Blenkinsop,* [1997;] *Hodge et al.,* [2018]), further suggesting that the foliation is not actively rotating stresses.

We therefore propose a variation of the *Morley,* [2010] hypothesis based on analogue models [*Corti et al.,* 2013; *Philippon et al.,* 2015]. Here, the regional principal stress axes [*sensu Pollard et al.,* 1993] in southern Malawi are uniformly parallel to those in Stress State 2, however, at the local scale [*sensu Twiss and Unruh,* 1998] fault slip vectors are rotated to dip-slip along the rift by a deep-seated weak ductile shear zone that is oblique to $\sigma_3$, but which conditions the geometry and distribution of the rift's faults (Figure 2e; *Hodge et al.,* [2018]; *Wedmore et al.,* [in prep.]; Figure 2e). The following constraints are therefore satisfied: (1) frictionally strong normal faults with a wide range of strikes are reactivated, (2) consistently oriented sets of N-S and E-W striking joints, (3) all faults have dip-slip kinematics. If true, this hypothesis has the following implications:

- A polymodal range of fault orientations at the southern end of the Malawi Rift (Figure 2a) can be accounted for by a uniform stress state and the Mohr Coulomb criterion, given that $\Phi$ is low and variably oriented pre-existing crustal weaknesses [c.f. *Healy* et al., 2015].
- Unlike in other rifts, variably striking faults in southern Malawi do not reactivate with faults striking orthogonally to $\sigma_3$ being linked by faults striking highly obliquely to $\sigma_3$. Instead, all faults can reactivate while striking slightly oblique to a uniformly E-W trending $\sigma_3$ (Figure 2e).
- Using fault slickensides and earthquake focal mechanisms in stress inversions is problematic as regional stresses and fault displacement are not necessarily aligned [*Philippon et al.,* 2015; *Twiss & Unruh,* 1998]. Furthermore, accurate principal stress directions will not be derived from stress inversions in which only a subset of fault orientations from a polymodal distribution are included [*Healy et al.,* 2015; *Twiss & Unruh,* 1998].
- This justifies a reassessment of the stress states and extension directions that have been inferred elsewhere in the Malawi Rift [*Chorowicz & Sorlien,* 1992; *Delvaux & Barth,* 2010; *Mortimer et al.,* 2007; *Ring et al.,* 1992], and other rifts where highly-oblique transfer zones have been proposed [e.g. *Chorowicz and Deffontaines,* 1993; *Acocella et al.,* 1999].
- Normal faults with a wide range of strikes can all reactive within the same stress state, which should be considered during seismic hazard assessment of continental rifts.

## 8. Conclusions

Attempts to determine the stress state in the Malawi Rift using fault geometry and slickensides [*Chorowicz & Sorlien,* 1992; *Mortimer et al.,* 2007; *Scott et al.,* 1992], earthquake focal mechanisms (Figure 3, *Delvaux and Barth,* [2010]), and geodetic models [*Saria et al.,* 2014; *Stamps et al.,* 2018] have produced ambiguous results. Therefore, to test the applicability of two possible stress states, we determined the reactivation potential of three representative differently-oriented faults in southern Malawi, in terms of their slip tendency, stress ratio, and effective coefficient of friction. The NW-SE striking Thyolo and Bilila-Mtakataka faults are well-oriented with respect to a stress state where $\sigma_3$ is SW trending (Stress State 1, Figure 2d). However, it is difficult to account for the reactivation of the unfavourably to severely misoriented NNE-SSW striking Chingale Step fault under Stress State 1, given realistic frictional properties of the rift ($\mu_s$~0.7, $P_f$ ~0). If $\sigma_3$ has a consistent

~E-W trend (Stress State 2, Figure 2e), all faults are favourably oriented to reactivate. An alternative hypothesis that fabrics actively rotate the stresses along the rift (Stress State 3, Figure 2f; *Morley*, [2010]), is inconsistent with spatially homogeneous joint orientations and local variations in the foliation orientation.

From this reactivation analysis, we consider that Stress State 2 is most applicable to southern Malawi, which is also consistent with regional joint sets (Figures 2 and 4) and large scale geodetic models [*Stamps et al.*, 2018]. This would suggest that all faults in southern Malawi reactivate by being slightly oblique (angle between fault strike and regional $\sigma_3$ trend <30°), and thus counter to typical models of oblique rifting in which one fault set strikes orthogonal to $\sigma_3$ and the other is highly oblique [*Acocella et al.*, 1999; *Bellahsen & Daniel*, 2005; *McClay & White*, 1995].

It is unclear whether the slightly oblique E-W extension predicted by Stress State 2 in southern Malawi is reflected in the fault's kinematics, or if the faults are actually pure dip-slip as indicated by the few well-determined focal mechanisms (Table 1). In the latter case, this inconsistency can be explained by a deep-seated zone of crustal weakness, which is exploited by the rift's faults and re-orients slip [*Corti et al.*, 2013; *Hodge et al.*, 2018; *Philippon et al.*, 2015]. Nevertheless, in rifts where stress states derived from measurements of fault displacement are ambiguous, fault reactivation potential analysis provides a powerful way to test their applicability.

## Acknowledgements

This research was funded by EPSRC Global Challenges Research Fund (grant number EP/P028233/1 'PREPARE'). Henri Leclère and Carolyn Boulton are thanked for providing codes to calculate the stress ratio of faults and guidance on how to use them. Antony Oldroyd conducted the XRD analysis and interpretation. All data is available from the corresponding author on request.

## References

Acocella, V., Faccenna, C., Funiciello, R., & Rossetti, F. (1999). Sand-box modelling of basement-controlled transfer zones in extensional domains. *Terra Nova*. https://doi.org/10.1046/j.1365-3121.1999.00238.x

Aldrich, M. J. (1986). Tectonics of the Jemez lineament in the Jemez Mountains and Rio Grande Rift ( USA). *Journal of Geophysical Research*. https://doi.org/10.1029/JB091iB02p01753

Allmendinger, R. W., Cardozo, N. C., & Fisher, D. (2013). *Structural Geology Algorithms: Vectors & Tensors*. Cambridge University Press, Cambridge, England.

Andreoli, M. A. G. (1984). Petrochemistry, tectonic evolution and metasomatic mineralisations of Mozambique belt granulites from S Malawi and Tete (Mozambique). *Precambrian Research*, *25*(1–3), 161–186. https://doi.org/10.1016/0301-9268(84)90031-7

Angelier, J., & Mechler, P. (1977). Sur une méthode graphice de recherche des contraintes principales également utilisable en tectonique et en séismologie: La méthode des dièdres droits. *Bulletin de La Société Géologique de France*, *7*(6), 1309–1318. https://doi.org/10.2113/gssgfbull.S7-XIX.6.1309

Bellahsen, N., & Daniel, J. M. (2005). Fault reactivation control on normal fault growth: An

573 experimental study. *Journal of Structural Geology*.
574 https://doi.org/10.1016/j.jsg.2004.12.003
575 Bellahsen, N., Fournier, M., D'Acremont, E., Leroy, S., & Daniel, J. M. (2006). Fault
576 reactivation and rift localization: Northeastern Gulf of Aden margin. *Tectonics*.
577 https://doi.org/10.1029/2004TC001626
578 Biggs, J., Nissen, E., Craig, T., Jackson, J., & Robinson, D. P. (2010). Breaking up the
579 hanging wall of a rift-border fault: The 2009 Karonga earthquakes, Malawi. *Geophysical*
580 *Research Letters*, *37*(11). https://doi.org/10.1029/2010GL043179
581 Bloomfield, K. (1958). The geology of the Port Herald Area. *Bulletin of the Geological*
582 *Survey, Malawi*, *9*.
583 Bloomfield, K. (1965). The Geology of the Zomba Area. *Bulletin of the Geological Survey,*
584 *Malawi*, *16*.
585 Bloomfield, K., & Garson, M. S. (1965). The Geology of the Kirk Range-Lisungwe Valley
586 Area. *Bulletin of the Geological Survey, Malawi*, *17*.
587 Bott, M. H. P. (1959). The mechanics of oblique slip faulting. *Geological Magazine*, *96*(2),
588 109–117.
589 Boulton, C., Barth, N. C., Moore, D. E., Lockner, D. A., Townend, J., & Faulkner, D. R.
590 (2018). Frictional properties and 3-D stress analysis of the southern Alpine Fault, New
591 Zealand. *Journal of Structural Geology*, *114*, 43–54.
592 https://doi.org/10.1016/j.jsg.2018.06.003
593 Bruhn, R. L., Parry, W. T., Yonkee, W. a, & Thompson, T. (1994). Fracturing and
594 hydrothermal alteration in normal fault zones. *Pure and Applied Geophysics*, *142*(3),
595 609–644. https://doi.org/10.1007/BF00876057
596 Brune, S., Willliams, S. E., & Müller, R. D. (2018). Oblique rifting: the rule, not the
597 exception. *Solid Earth*, *9*(5), 1187–1206. https://doi.org/10.5194/se-2018-63
598 Byerlee, J. (1978). Friction of rocks. *Pure and Applied Geophysics PAGEOPH*, *116*(4–5),
599 615–626. https://doi.org/10.1007/BF00876528
600 Caine, J. S., Bruhn, R. L., & Forster, C. B. (2010). Internal structure, fault rocks, and
601 inferences regarding deformation, fluid flow, and mineralization in the seismogenic
602 Stillwater normal fault, Dixie Valley, Nevada. *Journal of Structural Geology*, *32*(11),
603 1576–1589. https://doi.org/10.1016/j.jsg.2010.03.004
604 Castaing, C. (1991). Post-Pan-African tectonic evolution of South Malawi in relation to the
605 Karroo and recent East African rift systems. *Tectonophysics*, *191*(1–2), 55–73.
606 https://doi.org/10.1016/0040-1951(91)90232-H
607 Chorowicz, J., & Deffontaines, B. (1993). Transfer faults and pull-apart model in the
608 rhinegraben from analysis of multisource data. *Journal of Geophysical Research*.
609 https://doi.org/10.1029/93JB00190
610 Chorowicz, J., & Sorlien, C. (1992). Oblique extensional tectonics in the Malawi Rift, Africa.
611 *Geological Society of America Bulletin*, *104*(8), 1015–1023.
612 https://doi.org/10.1130/0016-7606(1992)104<1015:OETITM>2.3.CO;2
613 Corti, G. (2012). Evolution and characteristics of continental rifting: Analog modeling-
614 inspired view and comparison with examples from the East African Rift System.
615 *Tectonophysics*. https://doi.org/10.1016/j.tecto.2011.06.010
616 Corti, G., Philippon, M., Sani, F., Keir, D., & Kidane, T. (2013). Re-orientation of the
617 extension direction and pure extensional faulting at oblique rift margins: Comparison
618 between the Main Ethiopian Rift and laboratory experiments. *Terra Nova*, *25*(5), 396–
619 404. https://doi.org/10.1111/ter.12049
620 Craig, T. J., Jackson, J. A., Priestley, K., & Mckenzie, D. (2011). Earthquake distribution
621 patterns in Africa: Their relationship to variations in lithospheric and geological
622 structure, and their rheological implications. *Geophysical Journal International*, *185*(1),

403–434. https://doi.org/10.1111/j.1365-246X.2011.04950.x

Delvaux, D. (2001). Tectonic and palaeostress evolution of the Tanganyika-Rukwa-Malawi rift segment, East African Rift System. *Peri-Tethys Memoir 6: Peri-Tethyan Rift/Wrench Basins and Passive Margins*, 545–567.

Delvaux, D., & Barth, A. (2010). African stress pattern from formal inversion of focal mechanism data. *Tectonophysics*, *482*(1–4), 105–128. https://doi.org/10.1016/j.tecto.2009.05.009

Delvaux, D., & Sperner, B. (2003). New aspects of tectonic stress inversion with reference to the TENSOR program. *Geological Society, London, Special Publications*, *212*(1), 75–100. https://doi.org/10.1144/GSL.SP.2003.212.01.06

Dulanya, Z. (2017). A review of the geomorphotectonic evolution of the south Malawi rift. *Journal of African Earth Sciences*. https://doi.org/10.1016/j.jafrearsci.2017.02.016

Ebinger, C. J. (1989). Tectonic development of the western branch of the East African rift system. *Geological Society of America Bulletin*. https://doi.org/10.1130/0016-7606(1989)101<0885:TDOTWB>2.3.CO;2

Ebinger, C. J., Rosendahl, B. R., & Reynolds, D. J. (1987). Tectonic model of the Malaŵi rift, Africa. *Tectonophysics*, *141*(1–3), 215–235. https://doi.org/10.1016/0040-1951(87)90187-9

Ebinger, C. J., Deino, A. L., Tesha, A. L., Becker, T., & Ring, U. (1993). Tectonic Controls on Rift Basin Morphology: Evolution of the Northern Malawi (Nyasa) Rift. *Journal of Geophysical Research*, *98*(B10), 17821–17836. https://doi.org/10.1029/93jb01392

Engelder, T. (1985). Loading paths to joint propagation during a tectonic cycle: an example from the Appalachian Plateau, U.S.A. *Journal of Structural Geology*, *7*(3–4), 459–476. https://doi.org/10.1016/0191-8141(85)90049-5

Etheridge, M. A. (1986). On the reactivation of extensional fault systems. *Philosophical Transactions - Royal Society of London, Series A*. https://doi.org/10.1098/rsta.1986.0031

Fagereng, Å. (2013). Fault segmentation, deep rift earthquakes and crustal rheology: Insights from the 2009 Karonga sequence and seismicity in the Rukwa-Malawi rift zone. *Tectonophysics*, *601*, 216–225. https://doi.org/10.1016/j.tecto.2013.05.012

Flannery, J. W., & Rosendahl, B. R. (1990). The seismic stratigraphy of Lake Malawi, Africa: implications for interpreting geological processes in lacustrine rifts. *Journal of African Earth Sciences*, *10*(3), 519–548. https://doi.org/10.1016/0899-5362(90)90104-M

Fritz, H., Abdelsalam, M., Ali, K. A., Bingen, B., Collins, A. S., Fowler, A. R., et al. (2013). Orogen styles in the East African Orogen: A review of the Neoproterozoic to Cambrian tectonic evolution. *Journal of African Earth Sciences*. https://doi.org/10.1016/j.jafrearsci.2013.06.004

Habgood, F. (1963). The geology of the country west of the Shire River between Chikwaw and Chiromo. *Bulletin of the Geological Survey, Malawi*, *14*.

Habgood, F., Holt, D. N., & Walshaw, R. D. (1973). The geology of the Thyolo Area. *Bulletin of the Geological Survey, Malawi*, *22*.

Hamiel, Y., Baer, G., Kalindekafe, L., Dombola, K., & Chindandali, P. (2012). Seismic and aseismic slip evolution and deformation associated with the 2009-2010 northern Malawi earthquake swarm, East African Rift. *Geophysical Journal International*, *191*(3), 898–908. https://doi.org/10.1111/j.1365-246X.2012.05673.x

Hampel, A., Li, T., & Maniatis, G. (2013). Contrasting strike-slip motions on thrust and normal faults: Implications for space-geodetic monitoring of surface deformation. *Geology*. https://doi.org/10.1130/G33927.1

Hargrove, U. S., Hanson, R. E., Martin, M. W., Blenkinsop, T. G., Bowring, S. A., Walker, N., & Munyanyiwa, H. (2003). Tectonic evolution of the Zambezi orogenic belt: Geochronological, structural, and petrological constraints from northern Zimbabwe.

*Precambrian Research*. https://doi.org/10.1016/S0301-9268(03)00066-4

Healy, D., Blenkinsop, T. G., Timms, N. E., Meredith, P. G., Mitchell, T. M., & Cooke, M. L. (2015). Polymodal faulting: Time for a new angle on shear failure. *Journal of Structural Geology*. https://doi.org/10.1016/j.jsg.2015.08.013

Hellebrekers, N., Niemeijer, A., Fagereng, Å., Manda, B., & Mvula, R. (9999). Lower crustal earthquakes in the East African Rift System: Insights from frictional properties of rock samples from the Malawi Rift.

Henstra, G. A., Rotevatn, A., Gawthorpe, R. L., & Ravnås, R. (2015). Evolution of a major segmented normal fault during multiphase rifting: The origin of plan-view zigzag geometry. *Journal of Structural Geology*, *74*, 45–63. https://doi.org/10.1016/j.jsg.2015.02.005

Hodge, M., Fagereng, Biggs, J., & Mdala, H. (2018). Controls on Early-Rift Geometry: New Perspectives From the Bilila-Mtakataka Fault, Malawi. *Geophysical Research Letters*, *45*(9), 3896–3905. https://doi.org/10.1029/2018GL077343

Hodge, M., Biggs, J., Fagereng, Å., Elliott, A., Mdala, H., & Mphepo, F. (2019). A semi-automated algorithm to quantify scarp morphology (SPARTA): application to normal faults in southern Malawi. *Solid Earth*, *10*(1), 27–57.

Isaacs, A. J., Evans, J. P., Song, S.-R., & Kolesar, P. T. (2007). Structural, Mineralogical, and Geochemical Characterization of the Chelungpu Thrust Fault, Taiwan. *Terrestrial, Atmospheric and Oceanic Sciences*, *18*(2), 183. https://doi.org/10.3319/TAO.2007.18.2.183(TCDP)

Jackson, J., & Blenkinsop, T. (1997). The Bilila-Mtakataka fault in Malawi: an active, 100-km long, normal fault segment in thick seismogenic crust. *Tectonics*, *16*(1), 137–150. https://doi.org/10.1029/96TC02494

Jaeger, J. C., Cook, N. G., & Zimmerman, R. (2007). *Fundamentals of Rock Mechanics, 4th edition*. Wiley-Blackwell.

Johnson, S. P., De Waele, B., & Liyungu, K. A. (2006). U-Pb sensitive high-resolution ion microprobe (SHRIMP) zircon geochronology of granitoid rocks in eastern Zambia: Terrane subdivision of the Mesoproterozoic Southern Irumide Belt. *Tectonics*, *25*(6). https://doi.org/10.1029/2006TC001977

Kamb, W. B. (1959). Ice petrofabric observations from Blue Glacier, Washington, in relation to theory and experiment. *Journal of Geophysical Research*, *64*(11), 1891. https://doi.org/10.1029/JZ064i011p01891

Kolawole, F., Atekwana, E. A., Laó-Dávila, D. A., Abdelsalam, M. G., Chindandali, P. R., Salima, J., & Kalindekafe, L. (2018). Active Deformation of Malawi Rift's North Basin Hinge Zone Modulated by Reactivation of Preexisting Precambrian Shear Zone Fabric. *Tectonics*, *37*(3), 683–704. https://doi.org/10.1002/2017TC004628

Kröner, A., Willner, A. P., Hegner, E., Jaeckel, P., & Nemchin, A. (2001). Single zircon ages, PT evolution and Nd isotopic systematics of high-grade gneisses in southern Malawi and their bearing on the evolution of the Mozambique belt in southeastern Africa. *Precambrian Research*, *109*(3–4), 257–291. https://doi.org/10.1016/S0301-9268(01)00150-4

Laõ-Dávila, D. A., Al-Salmi, H. S., Abdelsalam, M. G., & Atekwana, E. A. (2015). Hierarchical segmentation of the Malawi Rift: The influence of inherited lithospheric heterogeneity and kinematics in the evolution of continental rifts. *Tectonics*, *34*(12), 2399–2417. https://doi.org/10.1002/2015TC003953

Leclère, H., & Fabbri, O. (2013). A new three-dimensional method of fault reactivation analysis. *Journal of Structural Geology*, *48*, 153–161. https://doi.org/10.1016/j.jsg.2012.11.004

Lisle, R. J., & Srivastava, D. C. (2004). Test of the frictional reactivation theory for faults

723 and validity of fault-slip analysis. *Geology*. https://doi.org/10.1130/G20408.1
724 Lisle, R. J., Orife, T. O., Arlegui, L., Liesa, C., & Srivastava, D. C. (2006). Favoured states of
725 palaeostress in the Earth's crust: evidence from fault-slip data. *Journal of Structural*
726 *Geology*, *28*(6), 1051–1066. https://doi.org/10.1016/j.jsg.2006.03.012
727 Lockner, D. A. (1995). Rock failure. *Rock Physics and Phase Relations: A Handbook of*
728 *Physical Constants*, *3*, 127–147.
729 Lopes Cardozo, G. G. O., & Behrmann, J. H. (2006). Kinematic analysis of the Upper Rhine
730 Graben boundary fault system. *Journal of Structural Geology*.
731 https://doi.org/10.1016/j.jsg.2006.03.010
732 Massironi, M., Bistacchi, A., & Menegon, L. (2011). Misoriented faults in exhumed
733 metamorphic complexes: Rule or exception? *Earth and Planetary Science Letters*,
734 *307*(1–2), 233–239. https://doi.org/10.1016/j.epsl.2011.04.041
735 McClay, K. R., & White, M. J. (1995). Analogue modelling of orthogonal and oblique rifting.
736 *Marine and Petroleum Geology*. https://doi.org/10.1016/0264-8172(95)92835-K
737 Moore, D. E., & Lockner, D. a. (2004). Crystallographic controls on the frictional behavior of
738 dry and water-saturated sheet structure minerals. *Journal of Geophysical Research*,
739 *109*(B03401), 1–16. https://doi.org/10.1029/2003JB002582
740 Morley, C. K. (2010). Stress re-orientation along zones of weak fabrics in rifts: An
741 explanation for pure extension in "oblique" rift segments? *Earth and Planetary Science*
742 *Letters*, *297*(3–4), 667–673. https://doi.org/10.1016/j.epsl.2010.07.022
743 Morley, C. K., Haranya, C., Phoosongsee, W., Pongwapee, S., Kornsawan, A., & Wonganan,
744 N. (2004). Activation of rift oblique and rift parallel pre-existing fabrics during
745 extension and their effect on deformation style: Examples from the rifts of Thailand.
746 *Journal of Structural Geology*, *26*(10), 1803–1829.
747 https://doi.org/10.1016/j.jsg.2004.02.014
748 Morris, A., Ferrill, D. A., & Henderson, D. B. (1996). Slip-tendency analysis and fault
749 reactivation. *Geology*. https://doi.org/10.1130/0091-
750 7613(1996)024<0275:STAAFR>2.3.CO;2
751 Mortimer, E. J., Paton, D. A., Scholz, C. A., Strecker, M. R., & Blisniuk, P. (2007).
752 Orthogonal to oblique rifting: Effect of rift basin orientation in the evolution of the
753 North basin, Malawi Rift, East Africa. *Basin Research*, *19*(3), 393–407.
754 https://doi.org/10.1111/j.1365-2117.2007.00332.x
755 Mortimer, E. J., Kirstein, L. A., Stuart, F. M., & Strecker, M. R. (2016). Spatio-temporal
756 trends in normal-fault segmentation recorded by low-temperature thermochronology:
757 Livingstone fault scarp, Malawi Rift, East African Rift System. *Earth and Planetary*
758 *Science Letters*, *455*, 62–72. https://doi.org/10.1016/j.epsl.2016.08.040
759 Muluneh, A. A., Kidane, T., Corti, G., & Keir, D. (2018). Constraints on fault and crustal
760 strength of the Main Ethiopian Rift from formal inversion of earthquake focal
761 mechanism data. *Tectonophysics*, *731–732*, 172–180.
762 https://doi.org/10.1016/j.tecto.2018.03.010
763 Nyblade, A. A., & Langston, C. A. (1995). East African earthquakes below 20 km depth and
764 their implications for crustal structure. *Geophysical Journal International*, *121*(1), 49–
765 62. https://doi.org/10.1111/j.1365-246X.1995.tb03510.x
766 Petit, C., Déverchère, J., Houdry, F., Sankov, V. A., Melnikova, V. I., & Delvaux, D. (1996).
767 Present-day stress field changes along the Baikal rift and tectonic implications.
768 *Tectonics*, *15*(6), 1171–1191. https://doi.org/10.1029/96TC00624
769 Philippon, M., Willingshofer, E., Sokoutis, D., Corti, G., Sani, F., Bonini, M., & Cloetingh,
770 S. (2015). Slip re-orientation in oblique rifts. *Geology*, *43*(2), 147–150.
771 https://doi.org/10.1130/G36208.1
772 Pollard, D. D., Saltzer, S. D., & Rubin, A. M. (1993). Stress inversion methods: are they

based on faulty assumptions? *Journal of Structural Geology*. https://doi.org/10.1016/0191-8141(93)90176-B

Price, N. J. (1959). Mechanics of jointing in rocks. *Geological Magazine*, *96*(2), 149–167. https://doi.org/10.1017/S0016756800060040

Ring, U., Betzler, C., & Delvaux, D. (1992). Normal vs. strike-slip faulting during rift development in East Africa: The Malawi rift. *Geology*, *20*(11), 1015–1018. https://doi.org/10.1130/0091-7613(1992)020<1015:NVSSFD>2.3.CO;2

Roberts, E. M., Stevens, N. J., O'Connor, P. M., Dirks, P. H. G. M., Gottfried, M. D., Clyde, W. C., et al. (2012). Initiation of the western branch of the East African Rift coeval with the eastern branch. *Nature Geoscience*, *5*(4), 289–294. https://doi.org/10.1038/ngeo1432

Sandwell, D., Mellors, R., Tong, X., Wei, M., & Wessel, P. (2011). Open radar interferometry software for mapping surface Deformation. *Eos, Transactions American Geophysical Union*. https://doi.org/10.1029/2011EO280002

Saria, E., Calais, E., Stamps, D. S., Delvaux, D., & Hartnady, C. J. H. (2014). Present-day kinematics of the East African Rift. *Journal of Geophysical Research: Solid Earth*, *119*(4), 3584–3600. https://doi.org/10.1002/2013JB010901

Scott, D. L., Etheridge, M. A., & Rosendahl, B. R. (1992). Oblique-slip deformation in extensional terrains: A case study of the lakes Tanganyika and Malawi Rift Zones. *Tectonics*. https://doi.org/10.1029/92TC00821

Sibson, R. H. (1985). A note on fault reactivation. *Journal of Structural Geology*, *7*(6), 751–754. https://doi.org/10.1016/0191-8141(85)90150-6

Sibson, R. H. (1998). Brittle failure mode plots for compressional and extensional tectonic regimes. *Journal of Structural Geology*, *20*(5), 655–660. https://doi.org/10.1016/S0191-8141(98)00116-3

Sibson, R. H., & Rowland, J. V. (2003). Stress, fluid pressure and structural permeability in seismogenic crust, North Island, New Zealand. *Geophysical Journal International*, *154*(2), 584–594. https://doi.org/10.1046/j.1365-246X.2003.01965.x

Stamps, D. S., Calais, E., Saria, E., Hartnady, C., Nocquet, J. M., Ebinger, C. J., & Fernandes, R. M. (2008). A kinematic model for the East African Rift. *Geophysical Research Letters*, *35*(5). https://doi.org/10.1029/2007GL032781

Stamps, D. S., Saria, E., & Kreemer, C. (2018). A Geodetic Strain Rate Model for the East African Rift System. *Scientific Reports*. https://doi.org/10.1038/s41598-017-19097-w

Sutherland, R., Toy, V. G., Townend, J., Cox, S. C., Eccles, J. D., Faulkner, D. R., et al. (2012). Drilling reveals fluid control on architecture and rupture of the Alpine fault, New Zealand. *Geology*, *40*(12), 1143–1146. https://doi.org/10.1130/G33614.1

Tenthorey, E., & Cox, S. F. (2006). Cohesive strengthening of fault zones during the interseismic period: An experimental study. *Journal of Geophysical Research: Solid Earth*, *111*(9). https://doi.org/10.1029/2005JB004122

Twiss, R. J., & Unruh, J. R. (1998). Analysis of fault slip inversions: Do they constrain stress or strain rate? *Journal of Geophysical Research: Solid Earth*. https://doi.org/10.1029/98JB00612

U.S. Department of the Interior U.S. Geological Survey. (2018). M 5.5 - 24km NE of Nsanje, Malawi [available at https://earthquake.usgs.gov/earthquakes/eventpage/us1000d1cy#executive, last accessed 26 Sept 2018].

Versfelt, J., & Rosendahl, B. R. (1989). Relationships between pre-rift structure and rift architecture in Lakes Tanganyika and Malawi, East Africa. *Nature*. https://doi.org/10.1038/337354a0

Wallace, R. E. (1951). Geometry of shearing stress and relation to faulting. *The Journal of Geology*, *59*(2), 118–130.

Walshaw, R. D. (1965). The Geology of the Nchue-Balaka Area. *Bulletin of the Geological Survey, Malawi*, *19*.

Wedmore, L., Biggs, J., Williams, J. N., Fagereng, Å., Dulanya, Z., Mphepo, F., & Mdala, H. (8888). Distributed active fault scarps in southern Malawi and the implications for the evolution of strain in amagmatic continental rifts.

Wheeler, W. H., & Rosendahl, B. R. (1994). Geometry of the Livingstone Mountains Border Fault, Nyasa (Malawi) Rift, East Africa. *Tectonics*, *13*(2), 303–312. https://doi.org/10.1029/93TC02314

Williams, J. N., Toy, V. G., Massiot, C., McNamara, D. D., Smith, S. A. F., & Mills, S. (2018). Controls on fault zone structure and brittle fracturing in the foliated hanging wall of the Alpine Fault. *Solid Earth*, *9*(2), 469–489. https://doi.org/10.5194/se-9-469-2018

Withjack, M. O., & Jamison, W. R. (1986). Deformation produced by oblique rifting. *Tectonophysics*. https://doi.org/10.1016/0040-1951(86)90222-2

## List of figures

Figure 1

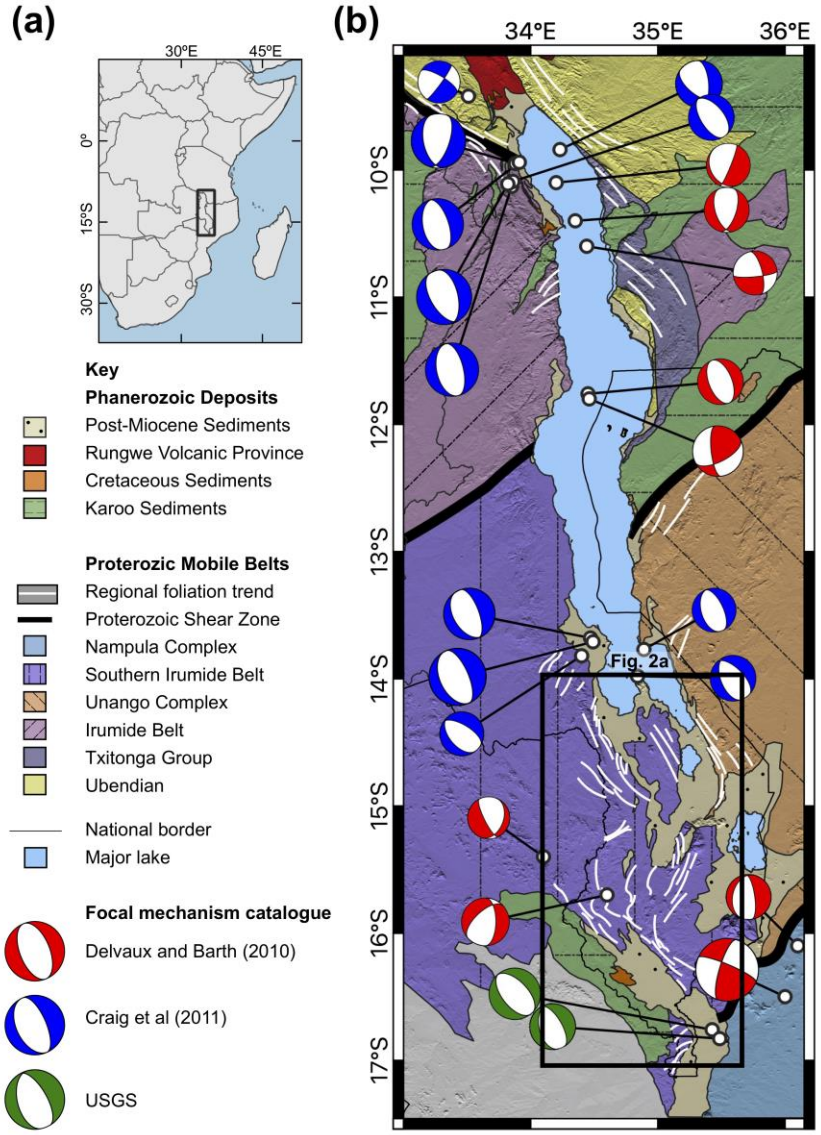


Figure 1: (a) Location of Malawi Rift within East Africa. (b) Simplified geological map of the rift with Proterozoic units taken from *Fritz et al.*, [2013], and underlain by Shuttle Radar Topography Mission (SRTM) 30 m digital elevation model (DEM; *Sandwell et al.*, [2011]). Location of focal mechanisms listed in Table 1 also given. Foliation orientations and trends collated from SRTM images, field measurements and previous studies [*Bloomfield*, 1958, 1965; *Bloomfield & Garson*, 1965; *Habgood et al.*, 1973; *Hodge et al.*, 2018].

Figure 2

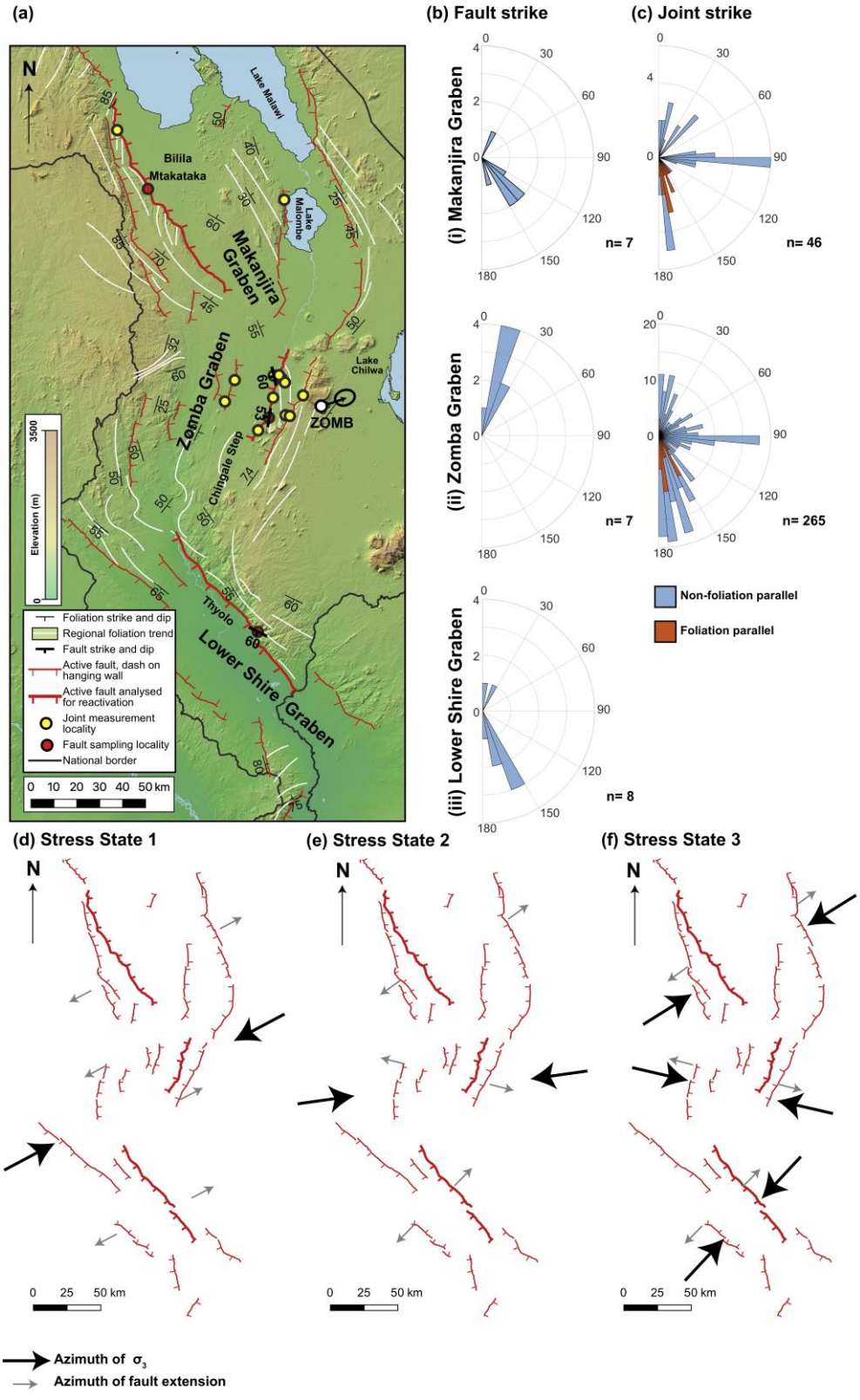


Figure 2: (a) Map of active faults in southern Malawi collated from TanDEM-X DEM and geological maps [*Bloomfield*, 1958, 1965; *Bloomfield and Garson*, 1965; *Walshaw*, 1965; *Habgood et al.*, 1973; *Hodge et al.*, 2018, 2019; *Wedmore et al.*, in prep.]. Area shown is indicated in Figure 1b. The azimuth of the ZOMB permanent GPS station is also shown [*Stamps et al.*, 2018]. Joint and fault

854 sampling and measurement localities also shown. Rose plots for measurements of (b) fault and (c)
855 joint strike for each of the grabens. Schematic representation of the $\sigma_3$ azimuth in Stress States (d) 1,
856 (e) 2, and (f) 3 with respect to faults in southern Malawi. In addition, we show extension direction as
857 inferred by the Wallace Bott criterion (for Stress States 1 and 3), or if a slip reorientation occurs (for
858 Stress State 2; *Philippon et al.*, [2015]). Area shown for each map is the same as in (a). Weighted
859 fault lines are those on which reactivation analysis was conducted.

860

861 Figure 3

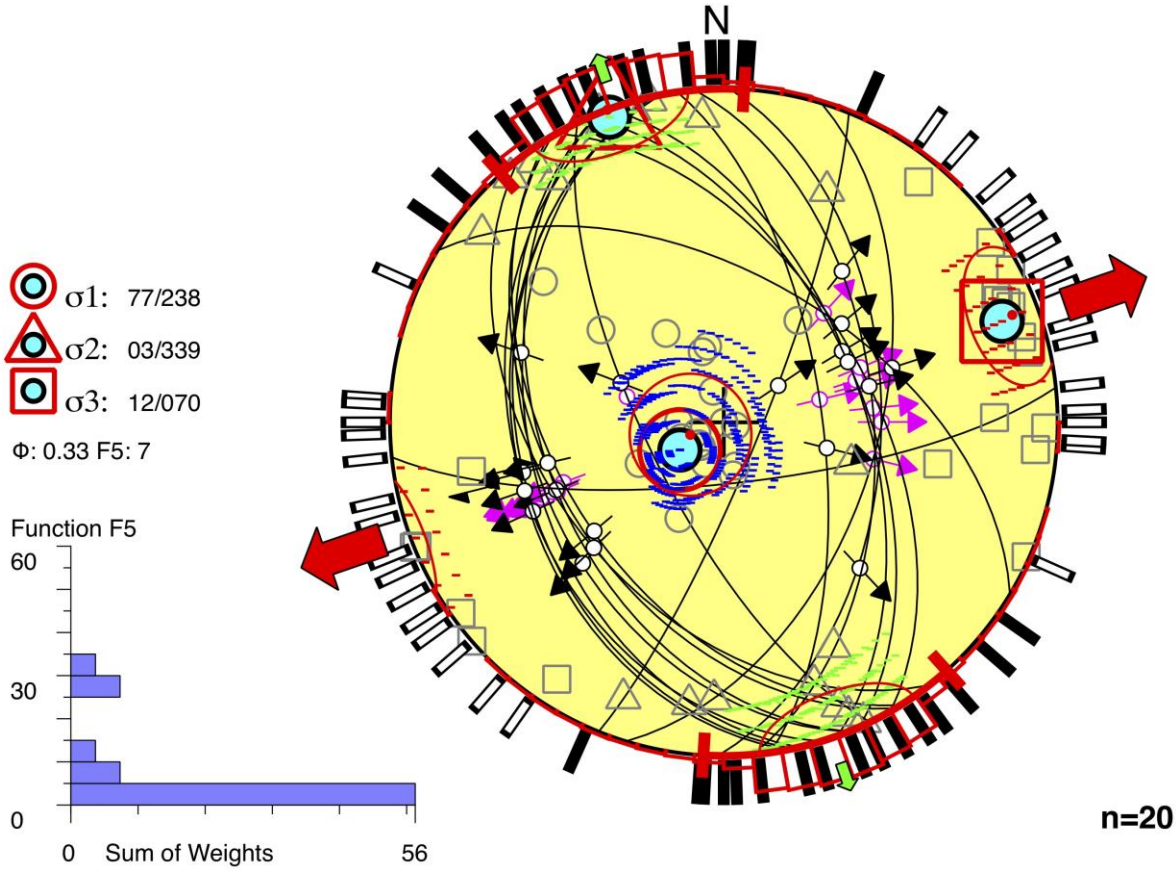


862
863 Figure 3: Results of earthquake focal mechanism stress inversion for the Malawi Rift using
864 Win-Tensor [*Delvaux & Sperner*, 2003] and the mechanisms listed in Table 1. Lower-
865 hemisphere equal area stereoplot depicts selected nodal planes (black lines) with slip vectors
866 (black arrows), the three principal stress axes (blue circles), maximum and minimum
867 horizontal stress ($S_{Hmax}$ and $S_{hmin}$) trajectories (small green and large red arrows), $S_{Hmax}$ and
868 $S_{hmin}$ trajectories for individual focal mechanisms (black and white bars outside stereplot),
869 and kinematic axes for individual focal mechanisms (grey circle: *p* axis, triangle: *b* axis,
870 square: *t* axis). Histogram represents distribution of misfit angles (ω), weighted arithmetically
871 according to magnitude.

872

873 Figure 4

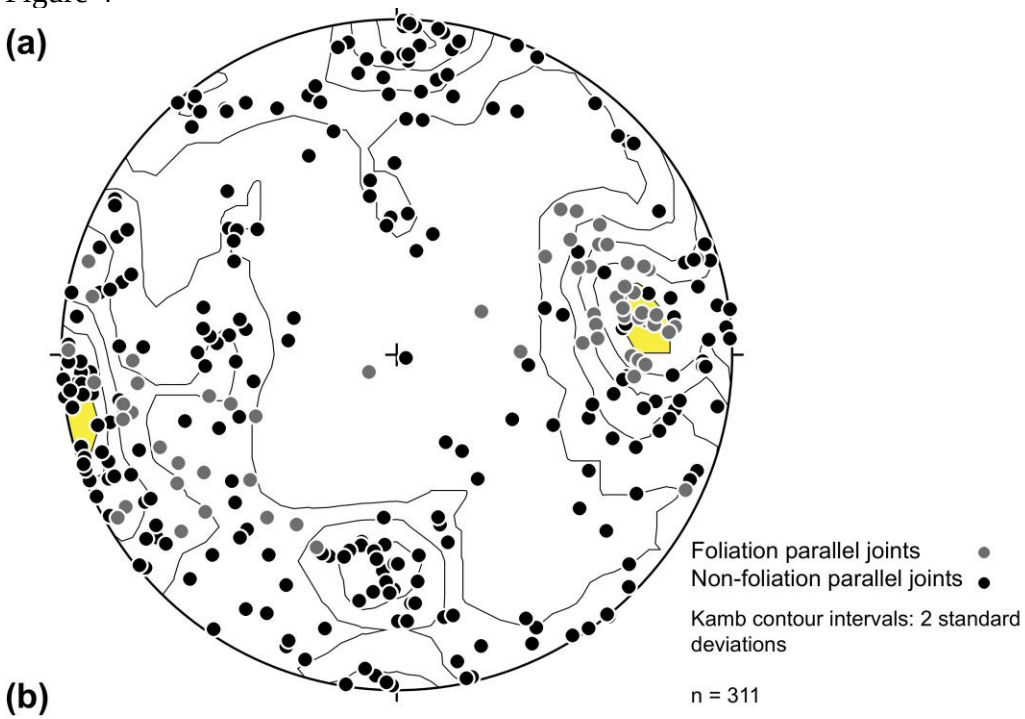


874
875 Figure 4: (a) Stereoplot showing poles to joint orientations that were also shown in Figure 2c.
876 Shaded contour interval indicates highest concentration of the N-S striking joints. The trend
877 at the centre of this interval (082°) is used to infer the trend of the minimum principal stress
878 ($\sigma_3$) for Stress State 2. The range of this interval ±7°. (b) Examples of joint sets in the Malawi
879 Rift. The joint set the facing the photo is a steeply dipping N-S set, which are mutually cross
880 cutting with an inclined E-W set.

881 Figure 5

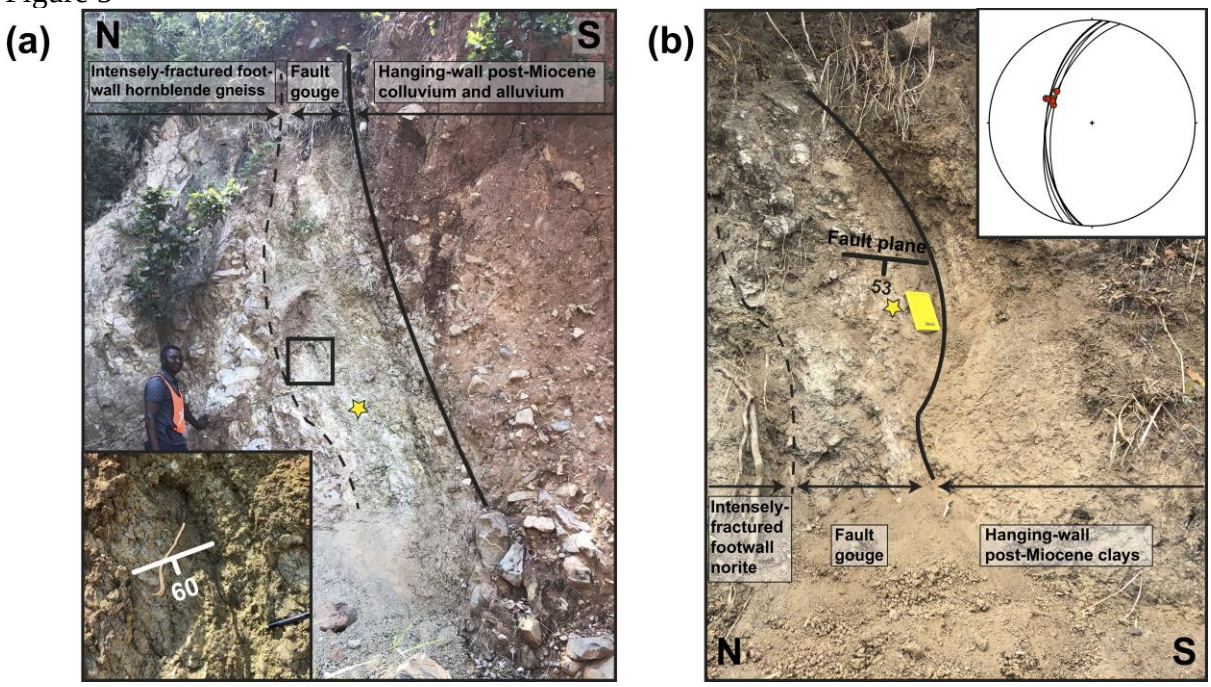


882

883 Figure 5: Examples of outcrops from (a) the Thyolo and (b) Chingale Step faults. Stars depict
884 where 'fault rock' samples were taken from for these faults. Footwall and hanging-wall unit
885 descriptions taken from *Habgood et al.,* [1973] and *Bloomfield,* [1965] respectively. Box in
886 (a) highlights plane that was used to measure dip of Thyolo fault and is shown in the inset.
887 Inset in (b) shows fault slickenside orientations [*Wedmore et al.,* in prep.]. Note, a dip of 57°
888 was used for the Chingale Step fault reactivation analysis, based on the average dip measured
889 over other sites (Figure 2a).

890

891 Figure 6

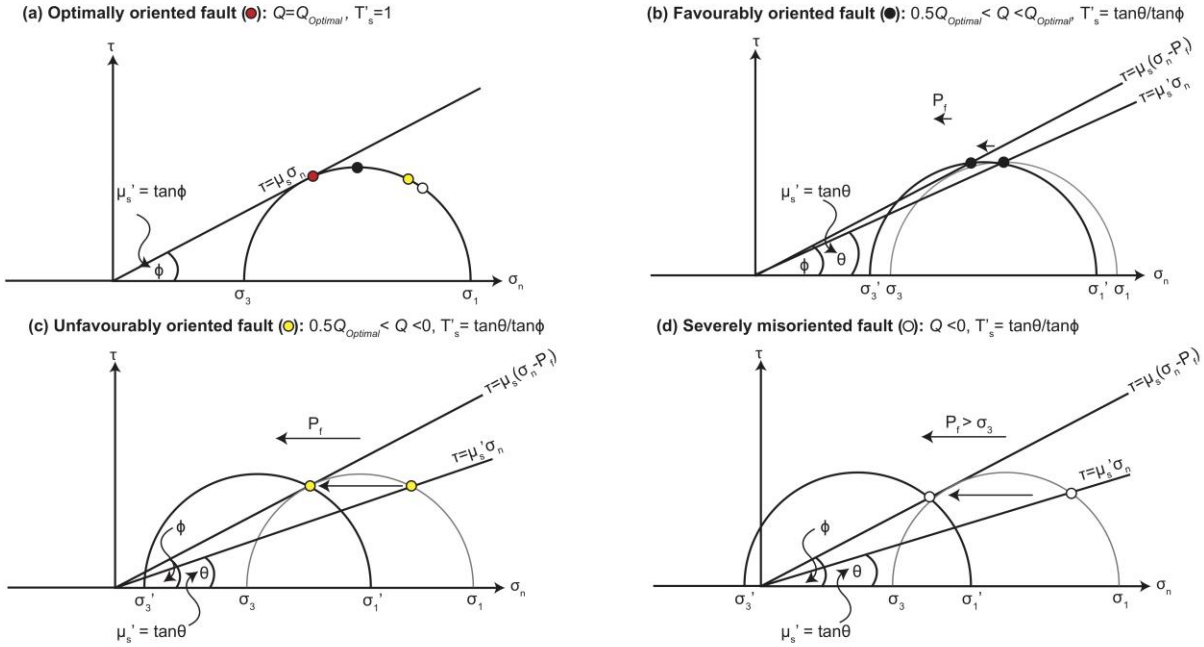


892

893 Figure 6: Illustration in Mohr Space of different concepts for analysing fault reactivation. (a)
894 The stress ratio ($Q$=$\sigma_3/\sigma_1$), normalized slip tendency ($T'_s$), and effective coefficient of friction
895 ($\mu_s$') acting on an optimally-oriented cohesionless fault. In this case, $Q = Q_{Optimal}$, $T'_s = 1$, $\mu_s$'
896 is the same as the frictional strength of an optimally oriented fault ($\mu_s$=tan$\phi$), and no fluid
897 pressure ($P_f$) is required for reactivation. In addition, the orientation of three hypothetical
898 faults is also depicted. The $Q$, $T'_s$, $\mu_s$', and $P_f$ required for reactivation of these (b) favourably
899 oriented, (c) unfavourably oriented, and (d) severely misoriented fault is then also shown. For
900 clarity, this example is for a 2D reactivation analysis when the fault plane contains $\sigma_2$.
901 However, the principles are the same for a 3D analysis.

902

903 Figure 7

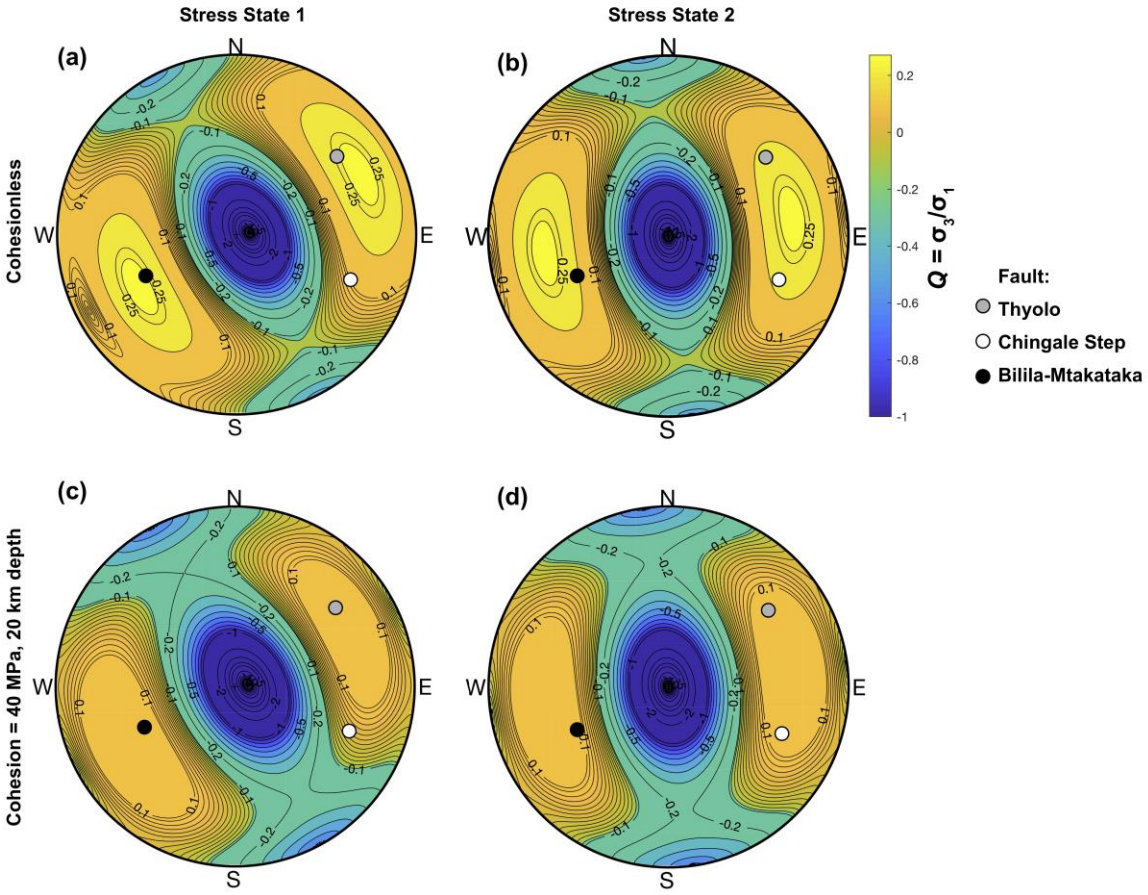


904

905 Figure 7: Stereoplots contoured by stress ratio ($Q$=$\sigma_3/\sigma_1$) required for fault reactivation in
906 Stress States 1 and 2 [*Leclère & Fabbri*, 2013]. Both (a&b) cohesionless and (c&d) cohesive
907 are considered. Results pertain to any depth for cohesionless faults and are calculated for a
908 depth of 20 km for cohesive faults, assuming the density model for the rift outlined in Table
909 S2. For all plots $\mu_s$=0.7 and $\Phi$=0.33. Poles to the fault orientations analyzed here are also
910 shown.

911

912 Figure 8

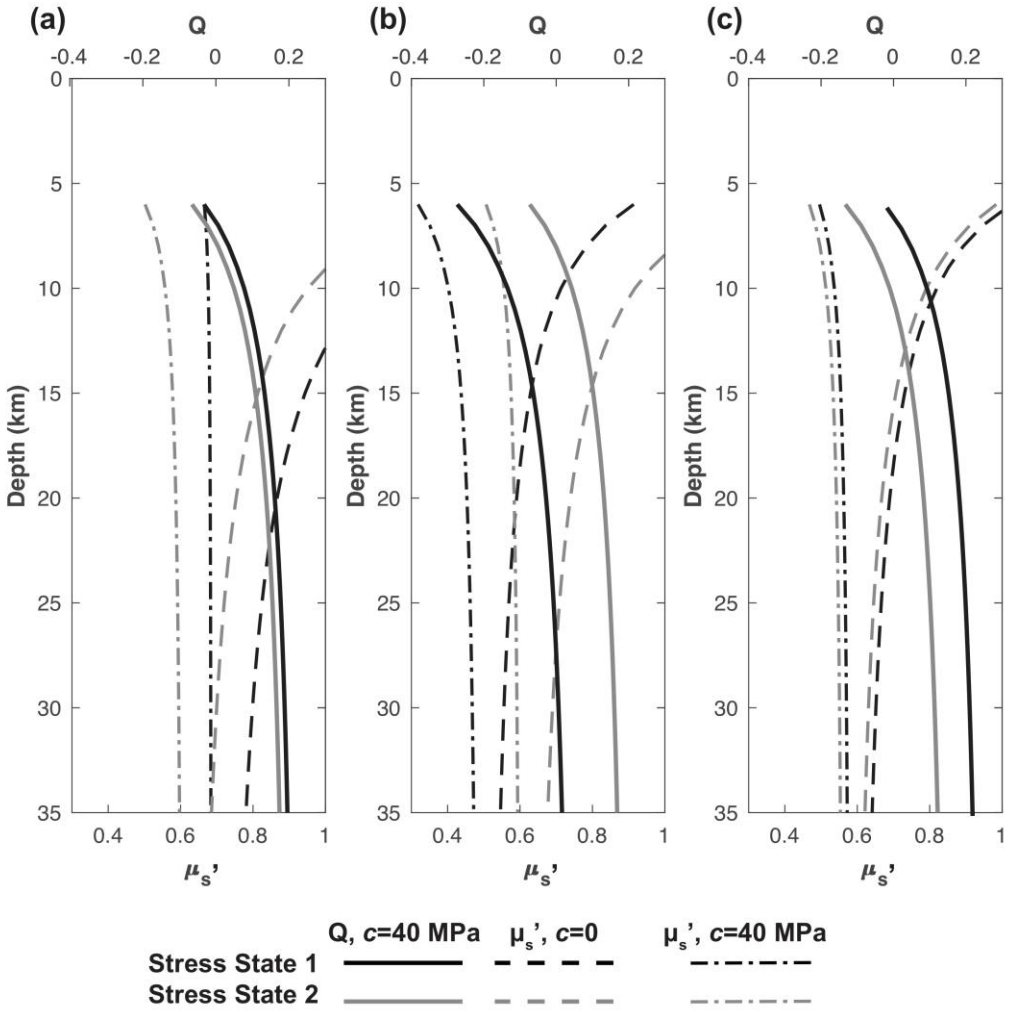


913

914 Figure 8: The stress ratio ($Q$=$\sigma_3/\sigma 1$) and effective coefficient of friction ($\mu_s$') of (a) Thyolo,
915 (b) Chingale Step, and (c) Bilila-Mtakataka fault for Stress States 1 and 2 between depths 6-
916 35 km. For cohesionless faults, $Q$ does not vary as a function of depth and so is not shown.
917 Only values where $\mu_s$'<1 are plotted.

918

919 Figure 9

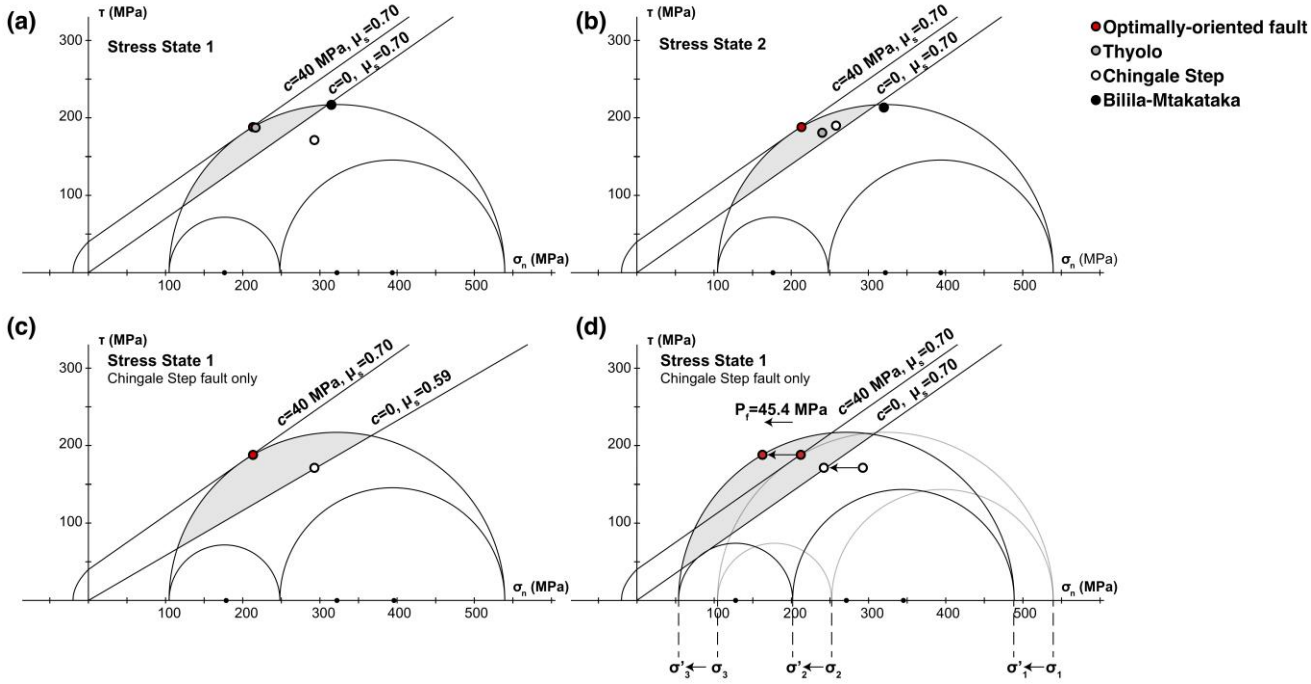


920

921 Figure 9: 3D Mohr Circle analysis for reactivation of faults in southern Malawi at 20 km
922 depth. Shaded region in each plot depicts range of orientations where a cohesionless fault will
923 reactivate. (a) Orientation of Thyolo, Chingale Step and Bilila-Mtakataka Fault in Stress
924 States 1. Given the failure criterions assumed here, only the Thyolo and Bilila-Mtakataka
925 fault will reactivate. (b) Same as (a) but for Stress State 2. The Thyolo and Chingale Step
926 faults will reactivate in this stress state and reactivation of Bilila-Mtakataka requires a slight
927 reduction in $\mu_s$' to 0.67 (Table 3). Reactivation of cohesionless Chingale Step fault in Stress
928 State 1 at 20 km depth requires that (c) $\mu_s$'=0.59 or that (d) $P_f$' = 45.4 MPa (equivalent to
929 $\lambda_v$'=0.08).

930

931 Figure 10

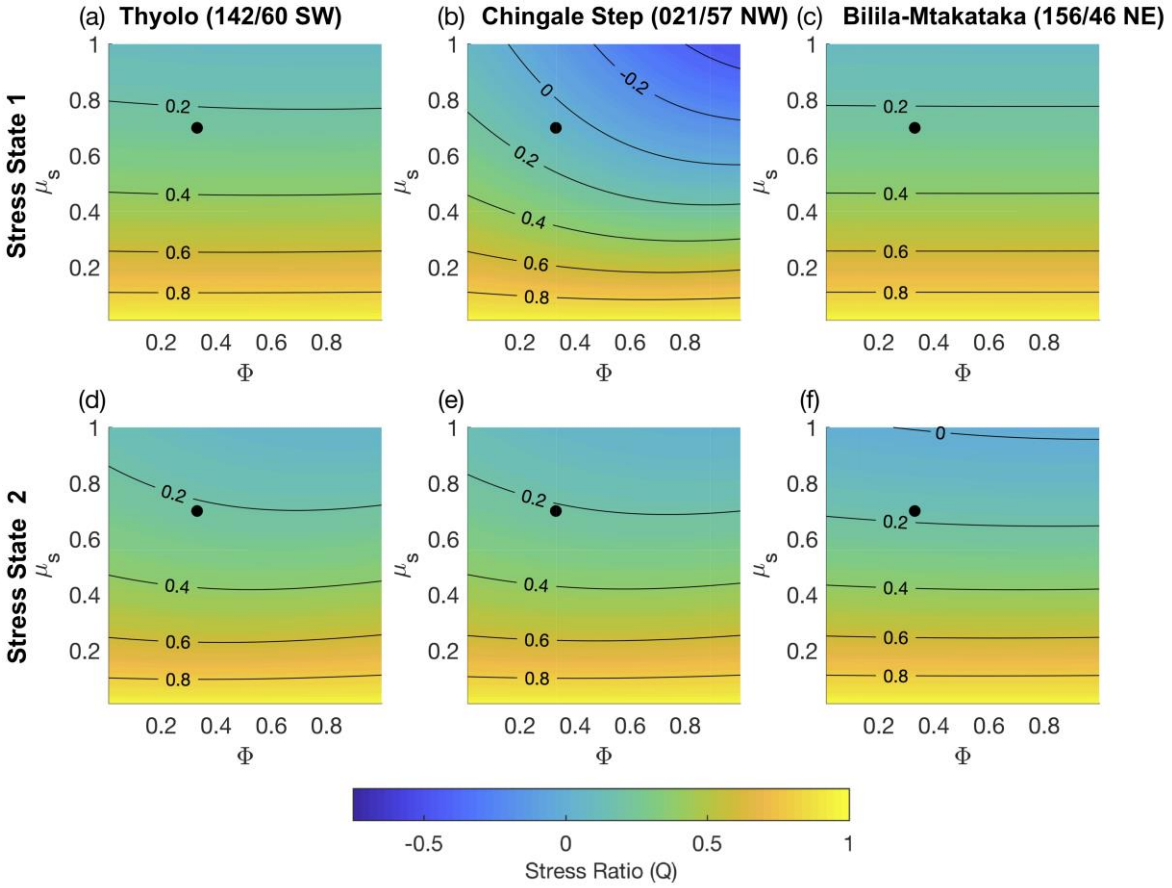


932

933 Figure 10: Contour plots for stress ratio ($Q=\sigma_3/\sigma_1$) needed for reactivation of a cohesionless
934 fault in frictional strength-stress shape ratio ($\mu_s$-Φ) space for the given fault orientations and
935 Stress States 1 and 2. Black circle represents point where Φ=0.33 and $\mu_s$=0.70, as is used in
936 Figure 7. For similar analysis for cohesive fault, see Figure S8.

937

938

939 **List of tables**

940 Table 1

| Date (yyyy/mm/dd) | $M_w$ | Longitude | Latitude | Depth (km) | Catalogue | Strike | Dip | Rake | Rejected | Misfit (°) | Notes |
|---|---|---|---|---|---|---|---|---|---|---|---|
| 1954/01/17 | 6.7 | 36.00 | -16.5.0 | 20 | DB2010 | 197 | 68 | 164 | Y | | |
| 1966/05/06 | 5.1 | 34.60 | -15.70 | 17 | DB2010 | 001 | 51 | -56 | | 31 | |
| 1978/01/08 | 4.9 | 34.45 | -11.76 | 15 | DB2010 | 338 | 45 | -90 | | 0 | |
| 1989/03/09 | 5.5 | 34.47 | -13.68 | 31 | C2011 | 340 | 56 | -99 | | 2.6 | Same as event 4 in DB2010 |
| 1989/03/10 | 6.1 | 34.49 | -13.71 | 32 | C2011 | 336 | 56 | -92 | | 1.2 | Same as event 5 in DB2010 |
| 1989/09/05 | 5.4 | 34.46 | -11.8 | 19.8 | DB2010 | 063 | 52 | 149 | Y | | |
| 1994/11/16 | 4.5 | 33.51 | -9.42 | 7 | C2011 | 301 | 64 | -11 | Y | | Focal mechanism from gCMT |
| 1995/07/22 | 4.9 | 34.84 | -13.98 | 33 | C2011 | 158 | 42 | -105 | | 7.3 | |
| 1995/09/30 | 4.7 | 34.40 | -13.82 | 30 | C2011 | 140 | 38 | -75 | | 2.4 | |
| 1996/08/30 | 4.5 | 34.10 | -15.40 | 10 | DB2010 | 071 | 27 | -46 | | 0.5 | |
| 1998/08/24 | 4.7 | 34.89 | -13.77 | 44 | C2011 | 163 | 37 | -95 | | 0.3 | Same as event 7 in DB2010 |
| 1999/09/01 | 4.7 | 34.2 | -10.10 | 10 | DB2010 | 022 | 81 | -144 | | 3.7 | |
| 2000/01/04 | 4.8 | 36.10 | -16.10 | 25 | DB2010 | 352 | 66 | -70 | | 3.7 | |
| 2002/08/31 | 5.0 | 9.84 | 34.23 | 20 | C2011 | 355 | 53 | -126 | | 28 | Same as event 9 in DB2010 |
| 2004/03/14 | 4.8 | 34.35 | -10.08 | 29 | DB2010 | 017 | 52 | -117 | | 13.6 | |
| 2004/08/21 | 4.7 | 34.44 | -10.60 | 12 | DB2010 | 084 | 75 | -17 | | 4.1 | |
| 2009/12/06 | 5.7 | -10.13 | 33.85 | 6 | C2011 | 168 | 38 | -91 | | 1.2 | |
| 2009/12/09 | 5.8 | -9.95 | 33.88 | 6 | C2011 | 167 | 41 | -70 | | 27 | |
| 2009/12/11 | 4.9 | -10.09 | 33.86 | 8 | C2011 | 148 | 48 | -96 | | 4.4 | Focal mechanism from gCMT |

| | | | | | | | | | |
|---|---|---|---|---|---|---|---|---|---|
| 2009/12/12 | 5.5 | -9.94 | 33.91 | 4 | C2011 | 169 | 37 | -95 | 0.4 |
| 2009/12/19 | 5.9 | -10.11 | 33.82 | 5 | C2011 | 149 | 46 | -77 | 1 |
| 2018/03/08 | 5.5 | 35.427 | -16.76 | 17 | USGS | 142 | 45 | -94 | 6.4 |
| 2018/03/08 | 4.9 | 35.486 | -16.83 | 10 | USGS | 330 | 54 | -77 | 1.6 |

Table 1: Compilation of earthquake focal mechanisms for the Malawi Rift. Catalogue codes are: (1) DB2010, *Delvaux and Barth*, [2010] and references therein, (2) C2011, *Craig et al.*, (2011) and references therein, (3) USGS, *U.S. Department of the Interior U.S. Geological Survey*, [2018]. Focal mechanisms from C2011 are from waveform modelling unless otherwise stated. The reported nodal plane is the one favoured by the stress inversion (i.e. the plane with the smallest misfist, the magnitude of which is also reported). We also indicate which mechanisms were filtered during the stress inversion. Map of focal mechanisms is given in Figure 1.

947 Table 2

| Fault | Sample | Quartz | Albite | Biotite | Muscovite | Actinolite | Kaolinite | Montmorillonite | Dolomite | Prehnite | Calcite |
|---|---|---|---|---|---|---|---|---|---|---|---|
| Thyolo | Country rock | 43 | 40 | | | 14 | 3 | | | | |
| | Fault rock | 81 | | | | | 8 | 5 | | 6 | |
| Chingale Step | Country rock | 30 | 30 | 37 | | | 3 | | | | |
| | Fault rock | 4 | | | | | | 2 | 1 | | 93 |
| Bilila-Mtakataka | Country rock | 11 | 52 | | 8 | 26 | 3 | | | | |
| | Fault rock | 74 | 16 | | | | | | | | 10 |

948 Table 2: Quantitative XRD (as weight %) of samples collected from fault zones in the Malawi Rift. Results are normalized to 100% and so do
949 not include estimates of unidentified or amorphous material. XRD diffractograms are given in Figure S5.

950

| **Fault** | **Fault orientation** | **Stress State** | **Stress Ratio (*Q*)** | | **Slip tendency ($T_s$)** | **Normalized slip tendency ($T'_s$)** | **Effective coefficient of friction ($\mu_s$')** | |
|---|---|---|---|---|---|---|---|---|
| | | | ***c*=0** | ***c*=40 MPa** | | | ***c*=0** | ***c*=40 MPa** |
| Thyolo | 142/60 SW | 1 | 0.24 | 0.16 | 0.65 | 0.92 | 0.87 | 0.68 |
| | | 2 | 0.22 | 0.14 | 0.61 | 0.87 | 0.75 | 0.59 |
| Chingale Step | 021/57 NW | 1 | 0.07 | -0.02 | 0.47 | 0.67 | 0.59 | 0.45 |
| | | 2 | 0.21 | 0.13 | 0.60 | 0.86 | 0.74 | 0.58 |
| Bilila-Mtakataka | 156/46 NE | 1 | 0.17 | 0.16 | 0.65 | 0.93 | 0.69 | 0.56 |
| | | 2 | 0.24 | 0.08 | 0.57 | 0.81 | 0.67 | 0.54 |

Table 3: Results of fault reactivation analysis in terms of the stress ratio (*Q*) of each fault with respect to Stress States 1 and 2, slip tendency ($T_s$), normalized slip tendency ($T'_s$), and effective frictional strength ($\mu_s$') needed to reactivate them. $T_s$, $T'_s$, and *Q* where c=0 pertain to any depth. *Q* where *c*=40 MPa and $\mu_s$' are for a depth of 20 km, and assume a fault surrounded by intact rock where $\mu_{s\text{-intact}}$=0.7. See Figure 8 for how these values vary with depth. All results to 2 decimal places.